UHASSELT

KNOWLEDGE IN ACTION

Faculteit Wetenschappen

master in materiomics

Masterthesis

Towards gold decorated hollow titania nanostructures: synthesis and optical properties of Au decorated polymer particles as template

Jarne Derkoningen

Scriptie ingediend tot het behalen van de graad van master in materiomics

PROMOTOR :

Prof. dr. Marlies VAN BAEL

Prof. dr. Pascal BUSKENS

2024
2025

UHASSELT

KNOWLEDGE IN ACTION

www.uhasselt.be
Universiteit Hasselt
Campus Hasselt:
Martelarenlaan 42 | 3500 Hasselt
Campus Diepenbeek:
Agoralaan Gebouw D | 3590 Diepenbeek

UHASSELT

KNOWLEDGE IN ACTION

Faculteit Wetenschappen

master in materiomics

Masterthesis

Towards gold decorated hollow titania nanostructures: synthesis and optical properties of Au decorated polymer particles as template

Jarne Derkoningen

Scriptie ingediend tot het behalen van de graad van master in materiomics

PROMOTOR :

Prof. dr. Marlies VAN BAEL

Prof. dr. Pascal BUSKENS

Towards gold decorated hollow titania nanostructures: synthesis and optical properties of Au decorated polymer particles as template

Jarne Derkoningen[1,], Esmee Roman[1,3], Sander Stulens[1,3], Ken Elen[1,2,3,4], Daniel Mann[1,2], Pascal Buskens[1,2], Marlies K. Van Bael[1,2,3,4]*

[1]Hasselt University, Institute for Materials Research (imo-imomec), DESINe team, Diepenbeek, Belgium

[2]The Netherlands Organisation for Applied Scientific Research (TNO), Eindhoven, The Netherlands

[3]imec, Institute for Materials Research (imo-imomec), Diepenbeek, Belgium

[4]EnergyVille, Genk, Belgium

E-mail: jarne.derkoningen@student.uhasselt.be, esmee.roman@uhasselt.be, sander.stulens@uhasselt.be, ken.elen@uhasselt.be, daniel.mann@tno.nl, pascal.buskens@tno.nl, marlies.vanbael@uhasselt.be

Key words: polymer templates, gold nanoparticles, gold nanoshells, localized surface plasmon resonance

Abstract

The conversion of CO_2 to CO, a valuable feedstock for further chemical synthesis, using the reverse water-gas shift reaction (RWGS) and sunlight as a sustainable energy source, is of interest to reduce CO_2 emissions. This makes plasmonic photocatalysts important. Here, hollow titania nanostructures decorated with gold nanoparticles or nanoshells are explored as catalysts for the light-powered RWGS reaction, aiming to establish the synthesis and investigate the optical properties. An emulsion polymerization is used to synthesize polystyrene and polymethyl methacrylate as template particles. Obtaining stable dispersions of particles with a narrow size distribution. Gold seeding is achieved via Sn^{2+} nucleation islands on the template surface. Colloidal stability during decoration of polymer particles with Au poses a challenge, requiring tailoring of reaction parameters. UV-Vis measurements show the localized plasmon resonance of the gold nanoparticles on the polymer particles, with an observed red shift because of the effect of the template's refractive index. Gold nanoshells are attempted to be made. TEM shows that no nanoshell is formed, but gold NP loading increases. Though the synthesis of the final Au decorated hollow TiO_2 nanostructures is not completed, the obtained results lay the foundation for further research on these types of systems.

Nederlandstalig abstract

De omzetting van CO_2 in CO, een waardevolle *feedstock* voor verdere synthese, met behulp van de *reverse water-gas shift reaction* (RWGS) en zonlicht als duurzame energiebron, is van belang om CO_2-uitstoot te verminderen. Dit maakt plasmonische fotokatalysatoren belangrijk. Hier worden holle titania nanostructuren gedecoreerd met gouden nanodeeltjes of *nanoshells* onderzocht als katalysatoren voor de door licht aangedreven RWGS-reactie, met als doel een synthese te bepalen en optische eigenschappen te onderzoeken. Een emulsiepolymerisatie wordt gebruikt voor de synthese van polystyreen en polymethylmethacrylaat als *template*-deeltjes. Er worden stabiele dispersies van monodisperse deeltjes verkregen. Goud *seeding* wordt bereikt via Sn^{2+} nucleatie-eilanden op het *template*-oppervlak. Colloïdale stabiliteit tijdens de decoratie van polymeerdeeltjes met Au vormt een uitdaging en vereist het aanpassen van de reactieparameters. UV-Vis-metingen tonen de gelokaliseerde plasmonresonantie van de gouden nanodeeltjes op de polymeerdeeltjes, met een waargenomen roodverschuiving vanwege het effect van de brekingsindex van het *template*. Er wordt geprobeerd om goud *nanoshells* te maken. TEM laat zien dat er geen *nanoshell* wordt gevormd, maar dat de goud nanodeeltjes-belading toeneemt. Hoewel de synthese van de uiteindelijke met Au gedecoreerde holle TiO_2-nanostructuren nog niet is voltooid, leggen de verkregen resultaten de basis voor verder onderzoek naar dit soort systemen.

1. Introduction

1.1. Background

Recent research indicates that global warming has indisputably been caused by the anthropogenic emission of greenhouse gases (e.g., CO_2 and CH_4). The observed differences in weather phenomena and extremes, like heat waves and droughts, are linked to anthropogenically caused climate change. Reduction of CO_2 emissions (and other greenhouse gas emissions) is required to mitigate anthropogenically caused climate change before reaching a tipping point.[1, 2]

Circular use of carbon can prevent further emissions of CO_2 into the atmosphere. CO_2 can be converted into chemicals or even back into fuels, minimizing net emissions and allowing carbon dioxide to serve as a feedstock. However, it is not only a circular use of carbon but a transition for the whole industry towards using more sustainable energy sources and feedstocks. Sunlight can be a sustainable energy source, and CO_2 and H_2 (when produced from renewable sources, viz. green H_2) can act as sustainable feedstocks in this new, transitioned industry. From this perspective, CO_2 becomes a new source for further synthesis of value-added chemicals.[3-6]

The conversion of CO_2 to CO is one of the main interests because of the versatility of CO. As a key component of syngas, carbon monoxide can serve as a feedstock for various products and chemicals, such as methanol and hydrocarbons. CO production is feasible via the reverse water gas shift (RWGS) reaction (**Scheme 1**), an endothermic reaction limited by equilibrium.[6-11]

$$CO_2 + H_2 \rightleftharpoons CO + H_2O \qquad \Delta H_{298K} = 41.2\ kJ{\cdot}mol^{-1}$$

Scheme 1. RWGS reaction

$$CO_2 + 4\ H_2 \rightleftharpoons CH_4 + 2\ H_2O \quad \Delta H_{298K} = -165.0\ kJ{\cdot}mol^{-1}$$

Scheme 2. Sabatier reaction

Thermo-catalysis of this reaction requires a temperature of over 700°C and a pressure higher than 2 MPa. Under these conditions, the equilibrium is shifted to CO formation, and the competing Sabatier reaction (**Scheme 2**) is suppressed. However, at these temperatures, CO production is accompanied by large energy consumption and catalyst degradation.[7-11]

Using an inexhaustible and emission-free source, *i.e.*, sunlight, in conjunction with a photocatalyst, has proven useful in executing such a reaction without conventional heating and avoiding excessive CO_2 emission due to inefficient use of energy.[7-10] Semiconducting metal oxides are often used as photocatalysts. These materials can use sunlight's energy to catalyze chemical reactions. Photons are absorbed in a semiconductor (SC) photocatalyst to generate electron-hole pairs, i.e., charge carriers, which can participate in chemical reactions. SC photocatalysis has been investigated extensively because of its wide application range and mild

reaction conditions (much lower temperature than thermo-catalysis). Despite this, stable oxidic semiconductors have some drawbacks: they primarily absorb the ultraviolet (UV) part of the solar spectrum, which only consists of a small part of the entire solar spectrum, and often significant charge carrier recombination rates are observed. These drawbacks result in a less efficient catalytic process and a lower performance of the SC photocatalyst.[11-14]

Recently, plasmon catalysis, which uses a broader region of the solar spectrum, mostly visible (Vis) and infrared (IR) light, has attracted more attention. Plasmonic metallic nanoparticles (NPs) interact with Vis light via a localized surface plasmon resonance (LSPR) effect. When the plasmonic metallic NPs are exposed to light with a frequency matching the so-called resonance frequency of the NPs, strong absorption of the light occurs. This results in a coherent oscillation of the free electron gas in the metal with the oscillating electric field of the incident light at the well-defined resonance frequency. The resonance frequency depends on the morphology/architecture, size, and composition of plasmonic particles and the refractive index of the surrounding medium. Plasmonic metallic NPs can, therefore, be tailored so that their plasmon resonance frequency is located in the Vis region of the solar spectrum.[6, 9, 10, 14-19] After plasmon excitation, which is the coherent oscillation of the free electrons, decay can occur in two ways. The plasmon can decay radiatively by emitting photons or by the excitation of electrons and holes. This results in the generation of so-called “hot charge carriers”. After a short period of time (~100 fs), these generated charge carriers will undergo relaxation via electron-electron and electron-phonon scattering. This ultimately leads to thermal dissipation.[20]

Unfortunately, applying these metallic NPs as photocatalysts, using the plasmonic effect as a direct way to drive the reaction, is not that efficient. The main reason is the mismatch of time scales: damping of the generated charge carriers in the metallic NP is in the order of femtoseconds; in contrast, charge injection to reactants is in the order of nanoseconds to milliseconds. For this reason, plasmonic metallic NPs are often combined with a semiconductive support, for instance TiO_2, leading to an increase in the lifetimes of the charge carriers and a more efficient catalyst system.[6, 9, 10, 14-18, 21]

Enhancement of the ‘NP on SC support’ catalyst system’s efficiency occurs via four effects.

(1) Enhancement of the local electric field: the metallic NP enhances the electric field around its exterior, leading to increased charge carrier generation in the SC.

(2) Hot electron injection: relaxation of the plasmon can generate hot electrons and holes in the metal NP. These hot electrons can pass through the Schottky junction at the

interface of the metal and the SC, trapping the electrons in the SC's conduction band (CB).

(3) Plasmon-induced resonance energy transfer (PIRET): through a strong dipole-dipole interaction between the metal NP and the SC, energy transfer occurs, generating charge carriers in the SC.

(4) Local heat generation: the hot charge carriers in the metal NP dephase via electron-electron and electron-phonon scattering. This results in heating the lattice and, consequently, the surroundings of the NP, which can enhance the reaction.

In conclusion, these four effects show that plasmonic metallic NPs are nano-sources of heat, electrons, and electromagnetic fields, locally increasing light absorption and temperature and improving the catalyst system's efficiency.[6, 9, 10, 14-18, 21]

The plasmon resonance frequency depends, among others, on the size of the nanoparticles. For spherical NPs, this dependence is limited. A weak variation is observed, meaning that only a small part of the Vis solar spectrum can be absorbed by spherical NPs.[17, 22, 23] This is shown in **Figure 1**. Spherical gold nanoparticles of different sizes were synthesized, and their optical properties were studied. It is shown that, despite significant size differences, there is little variation in the position of the band maximum. This indicates that the variation in plasmon resonance frequency of spherical NPs by size variation is limited.[23]

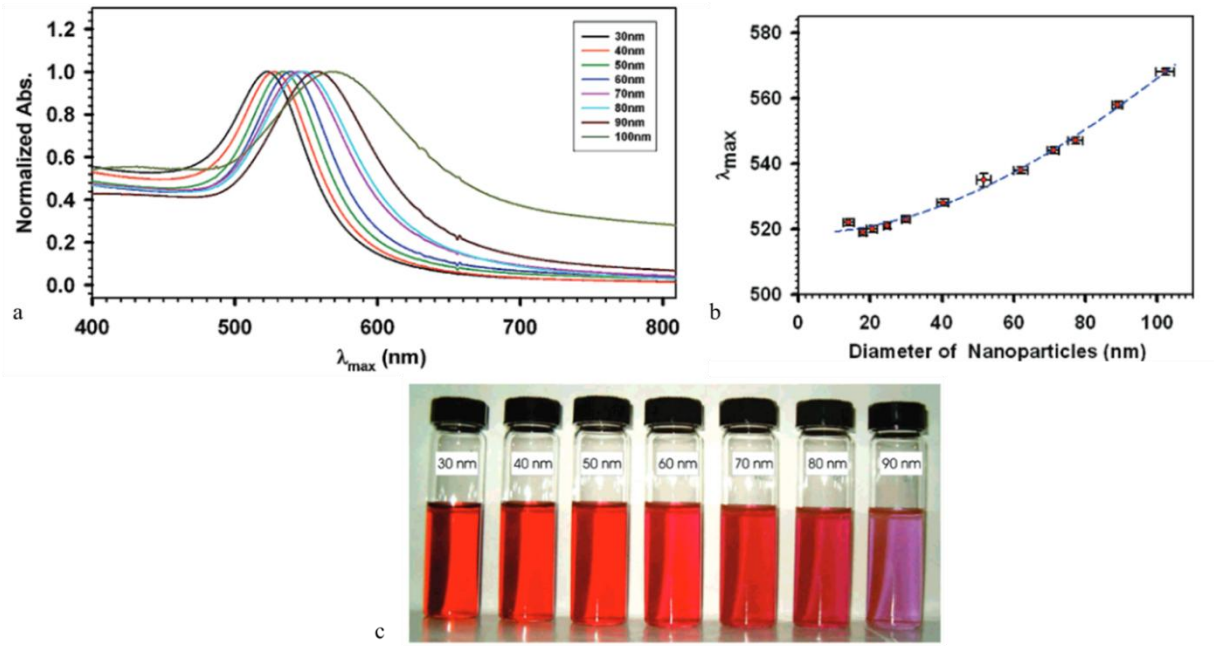

Figure 1. Normalized UV-vis spectra for gold nanoparticles in an aqueous solution, featuring different particle sizes. (a). Correlation between λ_{max} of the surface plasmon band and particle size of the Au nanoparticles (b). Photograph displaying the colors of gold nanoparticles in various particle sizes. (c). Graphs and photo taken and adapted from Reference 23.

Nanostructures with a plasmon resonance frequency tunable over a large part of the Vis and IR region of the solar spectrum are, for example, metallic nanoshells with a dielectric core. Here, the resonance frequency depends on the thickness and size of the metal shell, the core's dielectric constant, the core's diameter, and the surrounding medium.[22] The plasmon hybridization theory (**Figure 2**) describes the dependence of the resonance frequency of metallic nanoshells on these parameters.[22, 24-27]

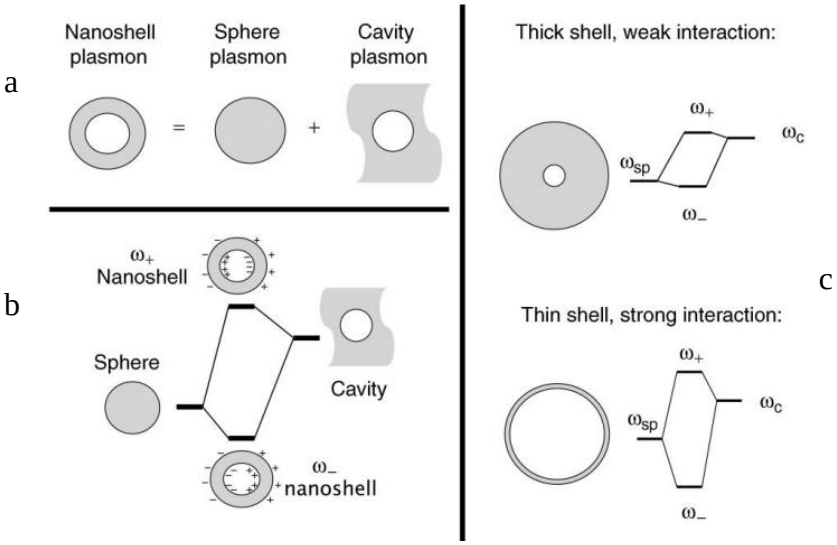

Figure 2. Plasmon hybridization model for nanoshells. (a) Combination of a nanosphere and a nanocavity results in a nanoshell. (b) Energy diagram of the interaction. (c) Interaction dependence on shell thickness. Figure taken and adapted from Reference 25.

In the plasmonic hybridization theory, the plasmonic response of the nanoshell can be seen as an interaction between a nanosphere and a nanocavity (Figure 2a). Just as in molecular orbital theory, the interaction results in a bonding plasmon (ω_-) and an anti-bonding plasmon (ω_+) (Figure 2b). Since the shell has a defined thickness, the two plasmons (surface charges) will interact. This directly indicates that the shell thickness can tune the interaction. A thicker shell will result in a weak interaction and, thus, less splitting of the plasmons; a thinner shell will result in a stronger interaction and, hence, more splitting of the plasmons (Figure 2c). Besides the shell thickness, the size of the shell (diameter) will also impact the resonance frequency. This model shows how this nanostructure can be engineered so that it is optimized to the emission spectrum of the light source.[22, 24, 25, 27]

As discussed above, combining a SC support with plasmonic NPs enhances the catalytic performance compared to the individual components. However, a limited tunability of the plasmon resonance frequency is observed for plasmonic NPs.

Engineering plasmonic nanoshells can allow greater tunability to absorb a more significant part of the solar spectrum. Engineering can be done by manipulating, for example, the shell thickness or the nanoshell size. However, these nanoshells are less interesting for catalytic applications. The interface of the metallic NP and the semiconductor has been recognized as the active site for the RWGS process.[28, 29] Covering the semiconductor fully with a nanoshell would remove the active sites, and fewer active sites would lead to a decreased catalytic activity.[30]

Plasmonic nanoshells are therefore less applicable for catalytic processes. The tunability of their plasmon resonance frequency makes them more interesting for optical applications. Nanoshells' optics have been investigated, and coupling between the inner surface and outer surface plasmons is observed; therefore, this has great application potential in plasmonic biosensors[22, 31, 32], photonic materials[26], and electronics[33].

Plasmonic NPs, especially Au, have drawn much attention because of their potential in catalytic applications.[7, 9, 11, 16, 17, 34, 35] A semiconductor photocatalyst is used as a support material because of the increased catalytic performance, including increased light absorption and charge carrier generation, and the trapping of hot electrons.[6, 9, 10, 14-18, 21]

Building on this concept of combining plasmonic catalysts with support materials, the use of Au as a plasmonic catalyst has been significantly investigated because of its high stability and absorption.[36] Gold's high stability mainly makes it favorable over other plasmonic metals, such as Ag, even though Ag has a higher absorption efficiency.[37] Titania, an n-type SC, has been extensively studied as a photocatalyst and support material because of its exceptional photocatalytic activity and photostability. CO production rates of these gold-titania systems have reached a value of 159.8 mmol $\cdot$ g_{cat}^{-1} $\cdot$ h^{-1}. Significantly higher than for systems where different plasmonic NPs (e.g., Cu, Rh, Pt) and different supports were used (e.g., CeO_{2-x}, Al_2O_3), indicating the promise of this system.[7, 11, 35, 38]

The photocatalytic activity can be further enhanced using hollow titania structures.[36, 39-41] Indeed, hollow titania structures affect the plasmonic NPs or nanoshells and photocatalytic performance. The incorporation of pores through hollow TiO2 spheres enables the adjustment of light penetration depth and thermal conductivity within the catalyst bed.[36, 39-41]

This way, the impact of light penetration depth and thermal conductivity can be systematically studied. Both light penetration depth and thermal conductivity of the whole catalyst material

play a vital role in the catalytic performance of the system, indicating the importance of achieving control over these parameters.[42, 43]

Hollow structures can be synthesized in a multitude of ways. Often, templating synthesis is used. Here, the templates function as temporary supports until the structure is completed. Once the synthesis is completed, the templates are removed, resulting in a hollow structure. Various template materials can be used, including polymers, SiO_2, and micelles.[41, 44] Often, a surface functionalization is required to obtain suitable compatibility between the template and the deposition material. Functional groups are often used.[41, 44] Here, the use of polymers as template material is discussed. Besides the synthesis of hollow structures, the templates can also be used for the deposition of gold NPs.[22, 45]

Polymer particles as templates have several advantages. Simple experimental procedures are required for the synthesis, narrow size distributions are common, and availability in large amounts with a wide range of sizes.[44] Calcination or extraction with a solvent is used to remove the template. A challenge here is to leave the formed shells around the template intact.[44]

To form shells or decorate the template particle, chemical deposition is often used and will be used here. Precursor metal ions are deposited on the template surface via electrostatic forces and then reduced to their metallic state. Precipitation in the form of a salt is also possible.[22, 44] The templates can also just function as a platform for a more controlled deposition of NPs, allowing for the tailoring of size, distribution, and surface coverage.[22, 44]

1.2. Aim of the project

There is still a need for a catalyst material allowing for the alteration of the porosity, which gives the ability to study the impact of light penetration depth and thermal conductivity on the catalytic performance towards the RWGS reaction. To our knowledge, hollow titania structures, combined with gold NPs or nanoshells, as catalyst systems in the RWGS reaction, and the optical properties of these systems have yet to be studied extensively. Therefore, the outlook of the project is to create hollow titania nanostructures incorporating gold NPs or nanoshells and investigate the impact of light penetration depth and thermal conductivity on their effectiveness as photocatalysts for the RWGS reaction. Gaining a deeper understanding of these systems could lead to developing new catalyst systems for the RWGS reaction, which could bring us closer to an efficient decrease in CO_2 emissions and a transition of the industry towards sustainable feedstocks and fuels.

The main objective of this research is to develop a synthesis route for polymer particles functioning as templates (see below), investigate a method for decoration with gold NPs, and establish a synthesis for gold nanoshells. Within this framework, two key research questions will be answered:

(1) Which polymer particles are suited for Au deposition, taking into account the fact that they merely serve as a template and need to be removed in a later stage? How can such polymer particles be synthesized in a controlled fashion (control of particle size, narrow size distribution)?

(2) What is a suited method for depositing Au nanoparticles and nanoshells on polymer particles, taking into account that control over Au particle size and loading, and random distribution of Au over the polymer particle surface are required?

A hard templating method will be used to synthesize the envisioned materials. In a first step, polymer particles will be synthesized in an emulsion polymerization. The particles will function as a template for the deposition of gold and titania in the following steps. Polystyrene (PS) and polymethyl-methacrylate (PMMA) will be used. PS will be used because it has already been shown that it can function as a template.[22, 46, 47] PMMA will be used because it has a lower ceiling temperature compared to PS (206°C for PMMA, 429°C for PS, at room temperature and 1 mol/l equilibrium monomer concentration).[48, 49] Also, PMMA should have a lower decomposition temperature and does not char, making the removal process less intense. The final step involves a template removal process.[41, 50] **Figure 3** depicts how the envisioned materials will be synthesized. An emulsion polymerization process in water will be used to synthesize polymer particles, functioning as hard templates in further steps (steps 1 & 1'). In steps 2 & 2', gold nanoparticles are grown on the polymer particles in a gold seeding step. After this, the workflow splits into two separate pathways. The upper path in Figure 3 applies an additional gold plating step, creating gold nanoshells on the polymer support (step 3). Titania is deposited on the nanoshells (step 4). Finally, a calcination step is carried out to remove the support particles (step 5). The lower path in Figure 3 skips the gold plating step (step 3') and immediately moves to the titania deposition (step 4'). After that, the calcination step is carried out (step 5').

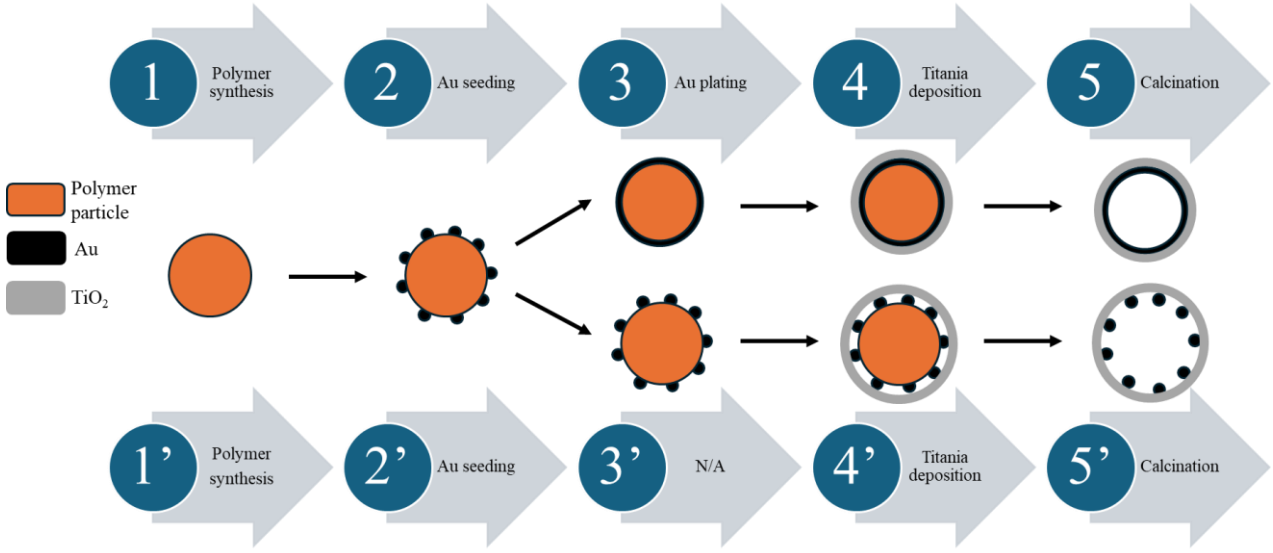

Figure 3. Workflow of the material synthesis.

The upper path is expected to result in hollow titania nanoparticles decorated with gold nanoshells. Whereas, the lower path is likely to result in hollow titania nanoparticles decorated with gold nanoparticles (Figure 3). The polymer synthesis, gold seeding, and gold plating steps will be based on methods developed by Mann D. and colleagues.[22, 46, 47]

It is hypothesized that PMMA particles can serve as suitable templates for Au deposition. The thermal properties are assumed to be beneficial in the removal process at the end of the synthesis.[48, 49, 51-53] PS can also serve as a suitable template, since it has been shown before.[22, 46, 47] But we expect that the template removal process is more difficult and would lead to less desirable results, like char remains. Controlled synthesis of the template particles is assumed to be obtainable via control over the parameters in the emulsion polymerization.[54] Here, the surfactant concentration will play a role. A smaller concentration leads to larger particles and to narrower size distributions.[54] Initial monomer concentrations also have an effect, with higher concentrations leading to larger particles, and vice versa.[54]

We hypothesize that functionalizing the template surface with Sn^{2+} ions, followed by the deposition of Au ions, reduction, and nucleation, will result in the formation of gold nanoparticles (NPs) that decorate the template particles.[22, 46, 47] Control over Au particle size and loading, and random distribution of Au over the polymer particle surface, is hypothesized to be obtainable via the ratio of the amount of Sn^{2+} to the amount of template material.[22, 46, 47]

2. Results and discussion

2.1. Synthesis of polymer particles

As discussed above, polymer particles were synthesized using an emulsion polymerization process in water. The polymer particles, PS and PMMA, act as hard templates for developing the hollow gold-decorated titania structures.[41, 50] Both processes used a Schlenk line setup and were similar in procedure (**Figure S1**). A Schlenk line is used to work under an Ar atmosphere. This prevents oxygen quenching of the radicals in the polymerization. After each synthesis, a milky-white dispersion, resembling latex, was obtained (**Figure S2** and **S3**). The suspension remained stable, showing no signs of flocculation for more than 3 months. Dynamic light scattering (DLS) was used to obtain particle sizes. **Table 1** shows the results. From these results, a narrow size distribution (Polydispersity index (PDI) <0.1[55]) is observed, except for measurement 1 of PS1. The applied method also shows good reproducibility; there is only slight variation between samples PS1-3 and PMMA1 and 2, which is attributed to experimental variations (**Table S1**).

For PS1-3, particle diameters around 50 nm are obtained. For PMMA1 and 2, diameters around 66 nm are obtained. The difference stems from the variation in the molar ratios of the monomers to surfactants in the PS and the PMMA synthesis. For PS, a monomer:surfactant ratio of 27:1 is used, whilst for PMMA, a ratio of 201:1 is used.[56, 57] The higher ratio leads to larger particles being formed.[54] Another factor that may play a role is the water solubility of the monomers. It is believed that the water solubility of the monomer influences the nucleation mechanism.[54] Because of the significantly higher water solubility of methyl methacrylate compared to styrene (35 times greater), it is more likely for a homogeneous nucleation mechanism to occur. In a homogeneous nucleation mechanism, the polymer particles will form in the aqueous phase, rather than in the micelles formed by the surfactant in a micellar nucleation mechanism. For homogeneous nucleation, the polymerization starts in the aqueous phase and continues until primary polymer particles are formed. These primary particles will coagulate, creating a sufficient hydrophobic interior to absorb monomers. Then, this coagulated particle will further grow. This contrasts with the micellar mechanism, where the micelles are present with a concentration much higher than the concentration of coagulated primary particles. In the micellar method, the primary particles, or shorter polymerized chains, will be absorbed into the micelles, where the polymerization will continue to form polymer particles. Lower coagulated particle concentrations in the homogeneous nucleation mechanism ultimately result in the formation of larger particles. However, in emulsion polymerization processes, it can be challenging to demonstrate that one nucleation mechanism is dominant over another.[54]

We tried to obtain larger particles with samples PS4 and 5 and PMMA 3 and 4, to investigate if this method could be easily adjusted to obtain size variations in the templates. To do this, the amount of monomer to surfactant was varied relative to the other syntheses.

With PS4, we halved the amount of surfactant, keeping the rest constant. In PS5 and PMMA3 and 4, the volume of monomer and water was doubled while the rest was kept constant (Table S1).

For PS4, no significant size increase is observed. The critical micelle concentration (CMC) of sodium dodecyl sulfate at 72°C is around $1.0 \cdot 10^{-2}$ M. The concentration of surfactant in the synthesis is 0.032 M, a factor of 3 higher than the CMC.[58] When the surfactant concentration is well above the CMC, the particle size is not as strongly dependent on surfactant concentration as compared to when the surfactant concentration is around the CMC. This explains the lack of increase in particle size and shows that the surfactant concentration should be varied substantially in order to observe variation in particle sizes.[54]

For PS5, an increase in particle diameter of around 20 to 30 nm is observed. This increase is attributed to the increased amount of monomer.[54] The surfactant concentration is still well above its CMC, so this should not have played a role.

For PMMA3 and 4, size increases of about 30 nm are observed in both syntheses, also stemming from the increased monomer concentration. The similar size increases are expected, since very similar reaction conditions were applied (Table S1). These results indicate that the processes can be altered straightforwardly, such that particle size variations are easily accessible.

Table 1. Particle diameters and PDI values obtained from DLS measurements on PS and PMMA.

Sample		1	2	3
PS1	Diameter [nm]	54.43	54.21	53.9
	PDI	0.112	0.068	0.051
PS2	Diameter [nm]	56.26	55.64	56.19
	PDI	0.05	0.056	0.035
PS3	Diameter [nm]	51.35	50.76	50.11
	PDI	0.034	0.053	0.059
PS4	Diameter [nm]	57.9	56.27	56.79
	PDI	0.035	0.076	0.031
PS5	Diameter [nm]	79.78	78.99	78.3
	PDI	0.026	0.047	0.055
PMMA1	Diameter [nm]	66.44	66.92	66.44
	PDI	0.067	0.047	0.028
PMMA2	Diameter [nm]	66.43	66.93	65.76
	PDI	0.075	0.056	0.038
PMMA3	Diameter [nm]	97.31	99.14	98.29
	PDI	0.055	0.053	0.002
PMMA4	Diameter [nm]	92.99	93.56	92.47
	PDI	0.081	0.064	0.075

Figure 4 depicts the transmission electron microscopy (TEM) images of PS1 and PMMA3. The other TEM images can be found in the Supporting Information (**Figure S4**). All TEM images show spherical particles, which is expected from the emulsion polymerization. The particle size of PS1 was quantitatively analyzed, as shown in **Table S2** and **Figure S5**. The average particle size was found to be 48.7 ± 0.8 nm with a 90% confidence interval. This measurement is smaller than the results obtained from DLS. The larger particle size determined by DLS is likely due to the fact that DLS measures the hydrodynamic radius. Due to inadequate or insufficient results, no quantitative analyses were performed on the other samples.

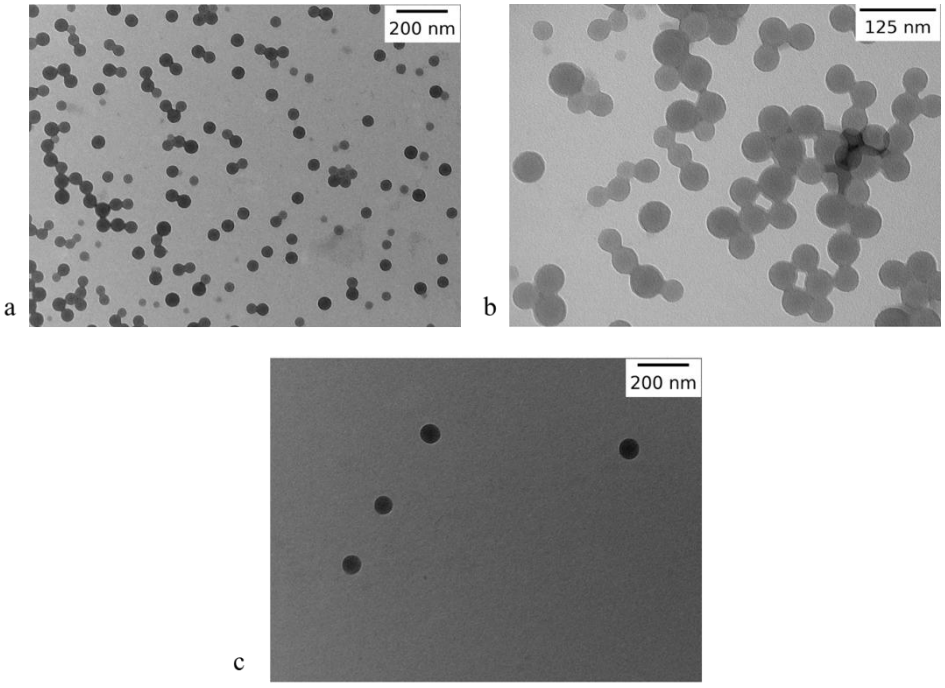

Figure 4. TEM images of samples PS1 (a), PS1 magnified (b), and PMMA3 (c).

The solid weight content was determined using a moisture analyzer, as shown in **Table 2**, and is an indicator of the yield of the synthesis. The PS samples showed a general decrease in solid weight content (and thus relative yield) with increasing sample number. This decrease could be due to experimental inconsistencies, but no definitive factor can be pointed out at this point to explain the results. The significantly lower relative yield for PS5 could be a consequence of the lower amount of initiator that was used in the synthesis (Table S1).[54] The PMMA samples exhibit comparable results across all samples, again indicating the reproducibility of the synthesis process.

Table 2. Solid content of each of the polymer samples.

Sample	Solid content [wt%]
PS1	20.36
PS2	19.27
PS3	19.77
PS4	18.87
PS5	17.92
PMMA1	17.23
PMMA2	16.46
PMMA3	17.71
PMMA4	17.64

To study the thermal stability and decomposition characteristics of PS and PMMA, thermogravimetric analysis (TGA) was conducted. **Figure 5** shows the TGA profiles, which align with existing literature.[52, 53, 59] The lower decomposition temperature in air for both polymers is because of oxidative degradation, whilst in N_2 atmosphere, pyrolytic degradation occurs for PS. PMMA depolymerizes because of the lower ceiling temperature.[48, 49, 60] Also, the profiles demonstrate that PMMA has a lower decomposition temperature compared to PS in both atmospheres and thus lower thermal stability (291.06°C in air and 337.92°C in N_2 for PMMA versus 358.95°C in air and 401.81°C in N_2 for PS). The absence of char formation in the degradation of PMMA makes it a promising template material. For PMMA, thermal degradation in N_2 atmosphere could suffice for complete removal, preventing the use of an oxidative atmosphere. Only the initial two steps outlined in Figure 3 were executed, so this assumption could not be tested.

In both profiles, a single-step weight loss is observed, so few other components are present, as expected. The evaporation of water is observed by a gradual weight loss starting around 100°C.

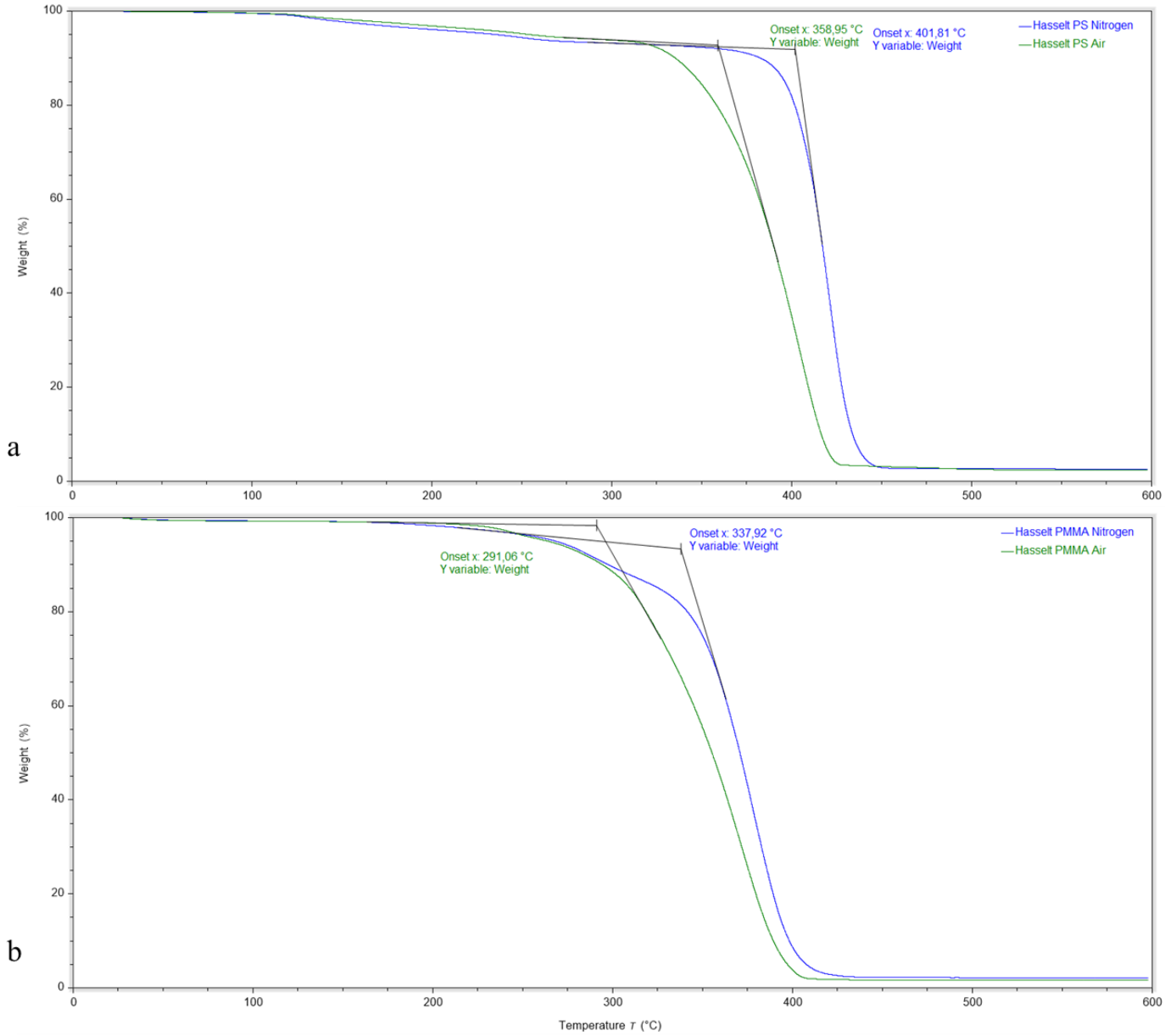

Figure 5. TGA profiles of PS (a), and PMMA (b).

Residual weights and the weight percentage are given in **Table S3**. For PS, residual weight percentages in nitrogen atmosphere and air of 2.575% and 2.477%, respectively, are obtained. For PMMA 2.092% and 1.623% in nitrogen atmosphere and air, respectively. The higher residual weight percentage for PS is attributed to char formation. PMMA has a lower ceiling temperature and undergoes depolymerization via an unzipping mechanism, leading to no or very little char formation.[48, 60] The residue weight is expected to mainly stem from inorganic content from the synthesis. Inorganic content may stem from potassium peroxodisulfate as initiator, and sodium dodecyl sulfate as surfactant. Both may leave inorganic content like sulfate salts.[61]

2.2. Gold seeding on polymer particles

2.2.1. Gold seeding on PS

Sample coding is indicated by "*(template sample) – Au – (x)*". The template sample is one of the synthesized samples from **Table S4**, Au indicates a gold seeding step, and x specifies the synthesis number. So, for the first seeding done on PS1, the sample code is PS1-Au-1. Table S4 shows all synthesized samples, together with the experimental parameters. **Figure S6** and **S7** depict the synthesized samples. The applied method is discussed in section 4.3.

A first seeding was done on sample PS1, and followed the procedure of Mann D., et al rigorously. The TEM images of PS1-Au-1 are shown in **Figure 6**a. The image shows a successful seeding, with an average particle size of 11.0 ± 0.4 nm (**Table 3**) obtained from the TEM analysis. Particle size distributions are depicted in **Figure S10**. The standard deviation in Table 3 indicates a significantly large variation in particle size, which is also observed visually in Figure 6a. This is attributed to the excess gold added, almost 3 times as much as the method described (Table S3), and the slight shortage of PS1 added (10.46 µl instead of 13.18 µl). Adjustment of both parameters is expected to lead to smaller gold NPs, together with more spread-out gold NPs.

For PS2-Au-1 (Figure 6b), the original method was abandoned because the amounts needed to be weighed in the original method were too small, so significant weighing errors were common. The use of stock solutions prevented this (**Table S5**). TEM images of PS2-Au-1 (Figure 6b) show that seeding is successful, with similar results compared to the first synthesis regarding the distribution of the gold NPs. Quantitative analysis shows that the average particle size is slightly smaller, 9.6 ± 0.4 nm (Table 3), than for PS1-Au-1. Since the confidence intervals do not overlap, it is assumed that the difference between the average particle sizes in these two samples is statistically significant. The difference is assumed to originate from the excess of gold added in the synthesis of PS1-Au-1. Adjustment of that synthesis, as discussed above, could lead to similar results for PS2-Au-1 and PS1-Au-1.

In hindsight, using a stock solution of $HAuCl_4 – K_2CO_3$ should not be favorable since it forms gold hydroxide, which is not desired in this step because of its lower solubility and reactivity towards reduction. For PS2-Au-1, this did not pose a problem, since fresh stock solutions were prepared and used in the synthesis. For other syntheses, this could have had an impact if an older stock solution was used. For future syntheses, it is proposed not to use stock solutions.

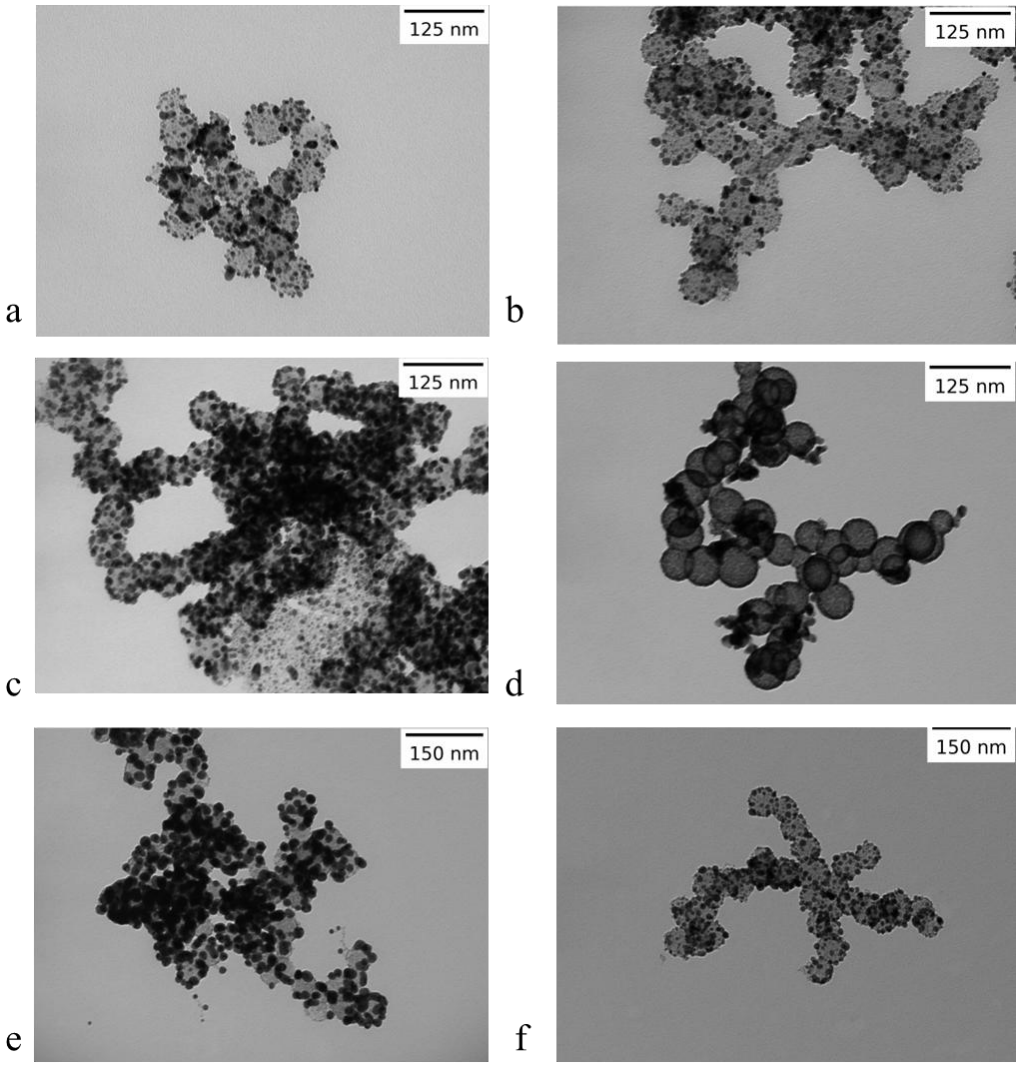

Figure 6. TEM images of samples synthesized with the original method PS1-Au-1 (a), PS2-Au-1 (b). And samples synthesized with the adapted method, PS1-Au-5 (c), PS1-Au-6 (d), PS1-Au-7 (e), and PS1-Au-8 (f).

Table 3. Quantitative TEM particle size analysis of PS1-Au samples and PS2-Au-1.

Sample	**Number of particles measured**	**Average particle size [nm]**	**Standard deviation [nm]**	**90% confidence interval [nm]**
PS1-Au-1	120	11.0	2.8	0.4
PS2-Au-1	123	9.6	2.7	0.4
PS1-Au-5	114	13.1	2.3	0.4
PS1-Au-7	81	18.2	2.8	0.5
PS1-Au-8	119	10.7	2.6	0.4

The applied method was scaled up. The motivation for this was to obtain larger amounts of gold-seeded polymer particles at the end of each synthesis, for analysis and potential further gold plating. The balance between the reactant amounts was not taken into account, leading to flocculation and unsuccessful seedings. A full discussion on the scaled-up version and the obtained results is given below. First, the adaptation of the method and the acquired results will be discussed, because it led to more desirable results.

The method for Au seeding was adapted, based on the articles of Mann D., et al.[22, 46, 47], to obtain a better balance between the reactant amounts. In this adaptation, the surface area and concentration of the template material are taken into account. In reference [46], seeding proved successful, with homogeneously distributed monodisperse NPs on the template surface. A ratio of 42 mg $SnCl_2$ per $4.0 \cdot 10^{16}$ nm² of template material (10.5 mg $SnCl_2/10^{16}$ nm² template material) is used in the synthesis. Here, we try to aim for this ratio (**Table S8**). Section 4.3.2 discusses the adaptation in detail for PS1, but it is analogous if other synthesized template materials are used.

The adapted method was used to synthesize samples PS1-Au-5 to PS1-Au-8, where syntheses 6,7, and 8 had slight variations in the method to study the effect on the outcome of the synthesis. In synthesis 6, no formaldehyde was used. In 7, only 100 µl of formaldehyde was used, instead of 200 µl. Synthesis 8 included using half as much gold ($HAuCl_4$) by doubling the other amounts (Table S4). No flocculation was observed in any of these syntheses. Figure 6c-f depicts the TEM images of these samples.

Figure 6c shows the TEM image of PS1-Au-5, the first synthesis with the adapted method. This result differs from PS1-Au-1, where the original method was used. An average particle size of 13.1 ± 0.4 nm (Table 3, Figure S10) is obtained, which is lower than for PS1-Au-1 (11.0 ± 0.4 nm). Also, fewer but larger gold NPs are observed per polymer particle (Figure 6c). The synthesis of PS1-Au-5 used 7.5 µl of PS1 (Table S4 and section 4.3.2). However, a more correct amount of PS1 (for 84 mg of $SnCl_2$) would be 3.71 µl. This amount would better correspond to the ratio that is aimed for: 42 mg $SnCl_2$ per $4.0 \cdot 10^{16}$ nm² of template material (see above and section 4.3.2). This increased amount of PS1 explains the obtained results. More template material results in fewer Sn^{2+} nucleation islands per particle. Gold seeding will result in deposition and growth of gold on these limited nucleation islands, resulting in larger particles, instead of smaller particles, more spread out over the particles if 3.71 µl had been used. The ratio of $SnCl_2$ to surface area of template material could not be calculated, but is expected to be similar to PS1-Au-6,7 and 8 (Table S8). By using 3.71 µl, the ratio would match the aimed ratio

of 10.5, and is expected to deliver the desired results: more and smaller particles, spread out homogeneously over the template surface.

Figure 6d shows the TEM image of sample PS1-Au-6, where no formaldehyde was used in the synthesis. It seems that the surface of the polymer particles is almost entirely covered in gold nanoparticles, despite no addition of reducing agent. Sn^{2+} can act as a reducing agent, which explains the full coverage of the particles' surfaces and the small size of the gold NPs. Also, it is possible that the sulfate chain-end groups have contributed to the reduction of the gold ions via a self-reduction mechanism on the PS surface.[62] The coverage may have been sufficient for the formation of a nanoshell; thus, UV-Vis spectroscopy was performed to analyze the optical properties. The results are discussed below.

For PS1-Au-7 (Figure 6e), the synthesis with half the amount of formaldehyde, an average particle size of 18.2 ± 0.5 nm is obtained (Table 3, Figure S10). From this, it is concluded that decreasing the amount of reducing agent leads to smaller particles. Also, the surface coverage of the template particle is much less. In other samples, a large number of gold NPs of various sizes can be observed on the template particle surface (Figure 6). For PS1-Au-7, the surface coverage by gold NPs is lower, but they are significantly larger in size.

PS1-Au-8 was synthesized with half the amount of gold ($HAuCl_4$). From Figure 6f, an average particle size of 10.7 ± 0.4 nm is derived (Table 3, Figure S10). This is significantly lower than the other syntheses, and is dedicated to the lower ratio of the amount of gold to the amount of template material.

Based on these results, it is concluded that when the amount of reducing agent (formaldehyde here) is decreased, the gold NPs increase in size, and as a consequence, the surface coverage by the NPs decreases. Also, by decreasing the amount of gold ($HAuCl_4$) that is added in the synthesis, the gold NP size can be decreased. When no reducing agent is added, the gold NPs become very small and evenly distributed (which is the ultimate goal) over the template surface.

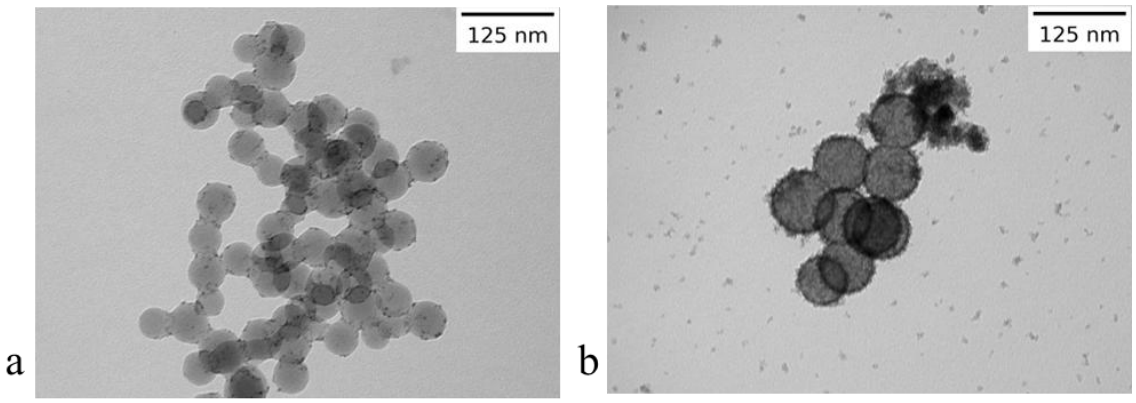

Figure 7. TEM images of samples synthesized with the scaled-up method. PS1-Au-3, and PS5-Au-9 (b).

As briefly mentioned above, the applied method was scaled up to obtain larger amounts of gold-seeded polymer particles at the end of each synthesis. However, the balance between the reactant amounts was not taken into account, leading to flocculation and unsuccessful seedings (**Figure S9**a-c). It is proposed that flocculation was due to a loss of electrostatic stabilization of the PS dispersion, once added to the $SnCl_2$-HCl solution. Sn^{2+} ions (and H^+ ions) adsorb on the negatively charged surface sites (sulfate chain-end groups), leading to a lower surface charge. This lower surface charge results in less strong electrostatic stabilization and thus flocculation.

The imbalance in the ratio between the reactant amounts can be seen in **Figure 7**a, TEM image of PS1-Au-3. Very small and few gold NPs are present, indicating few Sn^{2+} nucleation islands. This is also indicated by the low ratio of 0.00891 mg $SnCl_2/10^{16}$ nm² of PS1 (Table S8). The severe decrease in gold NP size is attributed to the scaling up of the synthesis: first, an increase of every parameter by a factor of 4 was done. Also, a switch was made from using 100 ml of a 2% formaldehyde solution to 21.64 ml of a 37% formaldehyde solution. Thereafter, the amount of template material was further increased, without changing the other parameters. In total, the amount was increased by a factor of 400, leading to 4.36 g of template material to be weighed (Table S4). This major increase in template material, without adjusting the amount of added tin and gold ($HAuCl_4$), is believed to be the cause of these results (Table S8). To try and obtain a better seeding, the amount of Sn^{2+} was increased.

With sample PS5-Au-9, 50 times the initial concentration of Sn^{2+} was used (Table S4). No flocculation occurred when adding the dispersion to the $SnCl_2$-HCl solution. It did occur when adding the Sn^{2+}-functionalized particles to the $HAuCl_4$-K_2CO_3 solution.

The TEM image of PS5-Au-9 in Figure 7b shows an almost complete coverage of the PS surfaces, accompanied by gold NPs in dispersion. The formation of gold NPs in dispersion stems from the fact that the sample was not centrifuged after Sn^{2+} functionalization, leading to Sn^{2+} in solution during the gold seeding step and thus gold NP formation in solution.

It is calculated that 1.02 mg $SnCl_2/10^{16}$ nm² PS5 was added (Table S8), which is much less than the aimed ratio of 10.5 mg $SnCl_2/10^{16}$ nm² template material (discussed at the start of page 21, Table S8). If the growth of the gold NPs is attributed to particle migration and coalescence, then the observed surface coverage is in line with the ratio.[62] A lower ratio results in fewer Sn^{2+} nucleation islands on the template particles, spread further apart from each other. Gold ions deposit and reduce on these nucleation islands. Because the nucleation islands are further apart from each other, the distance between them may surpass the diffusion length for nucleation and growth of the initially formed gold NPs, preventing further growth by particle migration and coalescence via kinetic limitations.

When the ratio increases, the distance between the nucleation islands decreases, which allows the growth of the initially formed gold NPs and reduces the surface coverage, leading to the results observed in Figure 6a-c and 6e-f.[62-64]

The TEM image also suggests that a nanoshell could have been formed. UV-Vis spectroscopy was done to investigate this further. The results of the UV-Vis measurements are discussed below.

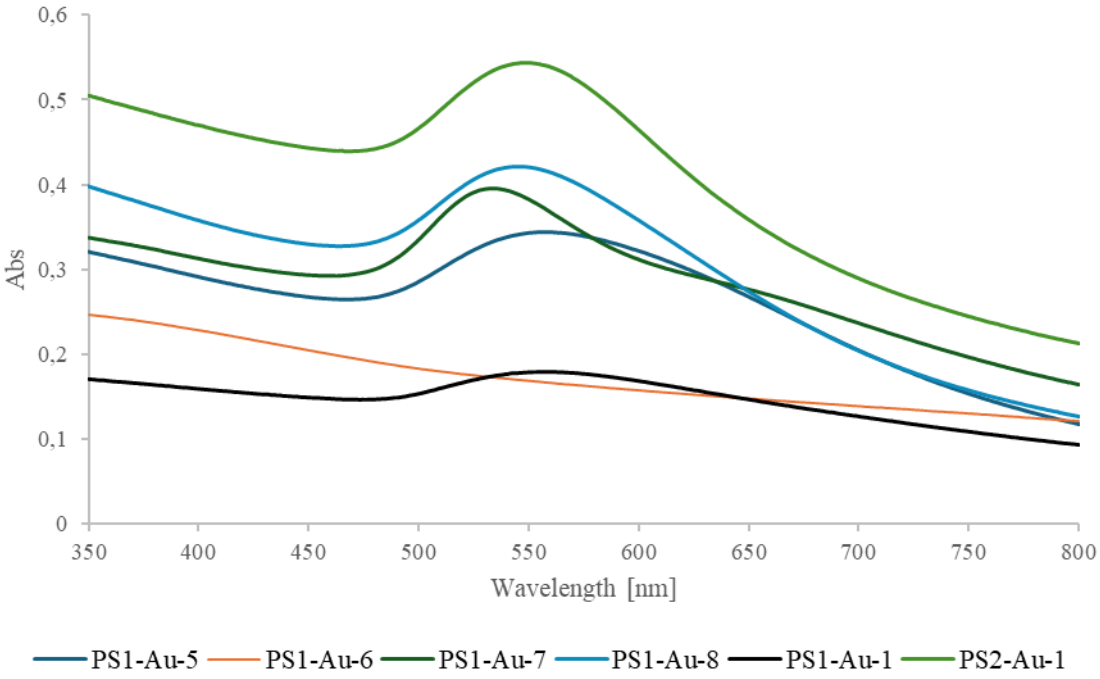

Figure 8. UV-Vis absorption spectra of samples PS1-Au-1,5,6,7,8 and PS2-Au-1.

Table 4. Wavelength of peak absorption for PS1-Au-1,5,6,7, and 8, together with the respective average particle sizes.

Sample	**Wavelength of peak absorption [nm]**	**Average particle size ± 90% confidence interval [nm]**
PS1-Au-1	560	11.0 ± 0.4
PS2-Au-1	549	9.6 ± 0.4
PS1-Au-5	559	13.1 ± 0.4
PS1-Au-7	534	18.2 ± 0.5
PS1-Au-8	546	10.7 ± 0.4

UV-Vis absorption spectra were measured to study the optical properties of the synthesized samples. **Figure 8** depicts the UV-Vis absorption spectra of the relevant samples discussed above. **Table 4** shows the wavelength of peak absorption for each sample in Figure 8, together with the respective average particle size. For PS1-Au-6, no peak absorption could be found using the applied method. The other spectra in Figure 8 do show a plasmon resonance band in the region of 540 nm, where it is expected for gold NPs.[22, 45, 65, 66]

However, all spectra are red-shifted compared to what is expected for gold NPs of these sizes; the wavelength of peak absorption is expected to be around 517 nm.[23, 45, 67] This can be attributed to the effect of the polymer template, PS. The surrounding medium's refractive index influences the gold nanoparticles' plasmon resonance. A larger refractive index leads to a red shift. Since PS has a larger refractive index than water, the plasmon resonance is red-shifted.[19, 22, 65]

PS1-Au-7 has a slight relative blue shift in its plasmon resonance, compared to the other spectra with similar resonances. The result is counterintuitive since a blue shift in the plasmon resonance is expected for smaller particles. Thus, we would expect a relative blue shift for PS2-Au-1, which is not observed.[22, 45, 65] When the size of the gold NPs is this small, intrinsic size effects come into play. As a result, the trends seen at larger particle sizes (generally > 25 nm), i.e., blue shift for smaller particle sizes and red shift for larger particle sizes, are not necessarily observed anymore. Inconsistent trends are observed, and no real size dependence can be noted. For the bandwidth, a theoretical and experimental correlation with the inverse of the (spherical) particle size (~ 1/R, R is the radius) has been observed. For larger particles, a smaller bandwidth can thus be expected. This explains the narrower peak for PS1-Au-7 in Figure 8.[65, 67]

The extensive bandwidth of PS1-Au-1 stands out among the bandwidths of the other samples with comparable particle sizes. Visually, a large variety in particle sizes is observed; the quantitative analysis, on the other hand, indicates similar varieties (standard deviation). It must be noted that the visual TEM analysis of a few clusters may not be representative of the whole sample; the same goes for the quantitative analysis of a (few) hundred gold NPs. The UV Vis spectrum indicates very small particles for PS1-Au-1 if taking intrinsic size effects into consideration, whilst intuitively, a large band width indicates a large size distribution. Both of which are observed experimentally (Figure 6 and S10), so we conclude that both have an effect in this case.[65, 67]

It was proposed that nanoshells could be formed in PS1-Au-6 and PS5-Au-9, but no plasmon resonance band(s) are observed in both cases.[22]

This could mean any of two things: one, the resonance band shifted out of the measured spectral range, or two, the system that was measured was too dilute to observe a resonance band.

The first hypothesis is discarded. Gold–silica nanoshells, consisting of a 120 nm silica template, coated with a 14 nm thick gold shell, show a wavelength at peak absorption near 800 nm. With decreasing shell size and with decreasing dielectric constant of the template material, the plasmon resonance shifts to lower wavelengths (blue shift). Since the template particles used in PS1-Au-6 and PS5-Au-9 are significantly smaller and have a lower dielectric constant, the plasmon resonance of the formed nanoshell should be visible in the spectral range. Also, small gold clusters are observed in the TEM images (Figure 6 and 7), and their plasmonic resonance should be visible. Both of these observations lead to the conclusion that the system was too dilute to observe a resonance band.[22]

2.2.2. Gold seeding on PMMA

PMMA was also studied as a template material for the gold seeding. Table S4 shows all synthesized samples, together with the experimental parameters. Figure S7 shows the synthesized samples for the PMMA template. **Figure S8** shows TEM images of some samples. Scale-up of the synthesis was carried out (Table S4) as discussed above. For the PMMA samples, flocculation proved to be a problem during the synthesis when the template dispersion was added to the $SnCl_2$-HCl solution, and no synthesis with a stable dispersion could be carried out. Initially, it was proposed that this flocculation was due to the lack of stability of the PMMA samples without considering any other effects. In retrospection, the flocculation of the PMMA samples probably also stemmed from an imbalance between the reactant amounts (Table S4 and S8).

Very low ratios were used (Table S8), far from the aimed ratio. These low ratios, together with high amounts of template material, probably resulted in the destabilization and the flocculation during the synthesis. To obtain better results, a higher ratio should be used. Either by increasing the amount of $SnCl_2$ used, or by decreasing the amount of PMMA. Both can also be done at the same time.

2.3. Gold plating on seeded polymer template particles

A gold plating step was tested on sample PS1-Au-5 (Figure 7a). **Table S6** shows the experimental parameters. **Figure 9** shows TEM images of the result of the synthesis. No full coverage of the PS' surface was obtained, and besides the gold NPs on the polymer particles, gold NPs in dispersion can also be observed. These stem from the use of $NaBH_4$ as a reducing agent, which can form gold nanoparticles in suspension. Separation via centrifugation was also difficult, also a reason for the non-deposited gold NPs' presence.

An average particle size of 11.6 ± 0.3 nm is obtained (**Table S7**, **Figure S17**). This is slightly lower than the average particle size in PS1-Au-5. It is observed that, rather than growing already deposited gold NPs, new gold NPs have formed on the surface of the template particles. This explains the observed decrease in average particle size. This is also indicated by the absorption spectrum in **Figure 10**, which has a wavelength of peak absorption at 529 nm and a sharper peak.

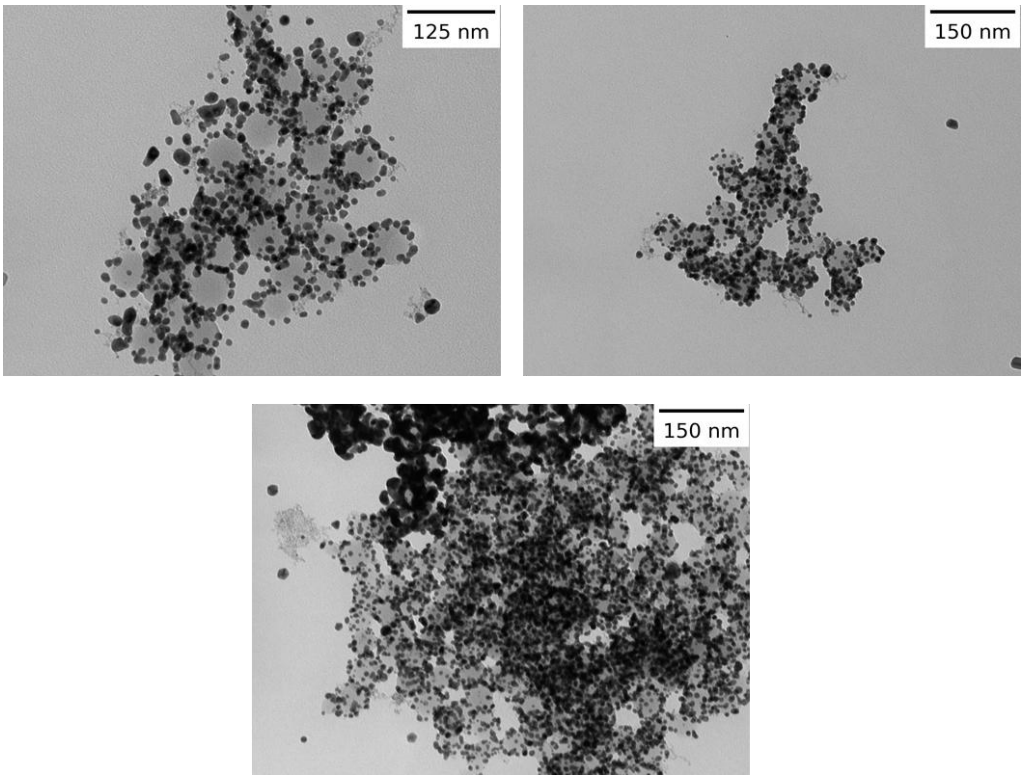

Figure 9. TEM images of the gold plating on PS1-Au-5 (PS1-Au-5-NS).

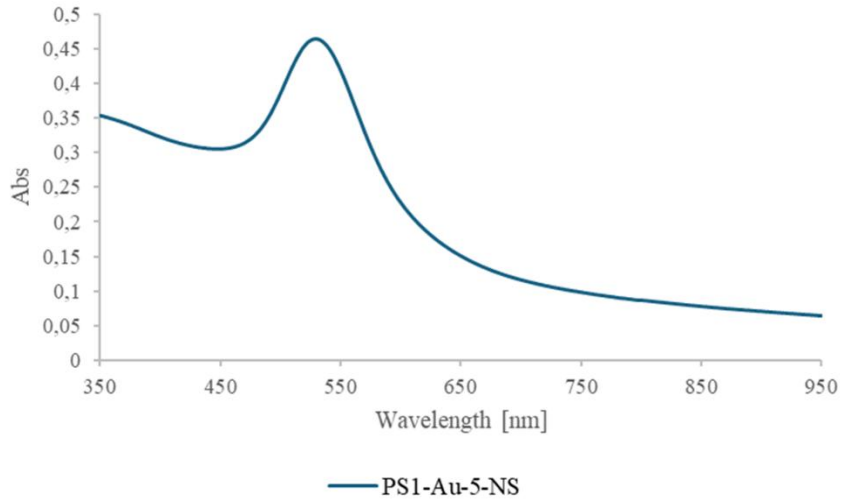

Figure 10. UV-Vis absorption spectrum of sample PS1-Au-5-NS.

3. Conclusion and outlook

This study aimed to develop a synthesis method for polymer particles functioning as templates, investigate a method for decoration with gold NPs, and establish a synthesis for gold nanoshells. The first step in the process, the synthesis of template particles, was successfully carried out. Stable dispersions and monodisperse PS and PMMA particles, with particle diameters of 50-55 nm for PS and around 66 nm for PMMA, were obtained via an emulsion polymerization of styrene and methyl methacrylate. Size variation proved possible via variation in the ratio of monomer to surfactant, allowing for a size increase of about 20 nm for PS and 30 nm for PMMA. A controlled synthesis of these particles is obtainable via variation in the amount of monomer. A larger amount of monomer leads to larger particles. This partly confirms our hypothesis. Surfactant concentration plays a smaller role than expected when the concentration is significantly larger than the CMC. Initial monomer, however, does play a significant role. Analysis of the thermal properties showed that PMMA has a lower thermal stability and does not char, both of which are desired properties for a template removal process. It was hypothesized that PMMA can serve as a suitable template for Au deposition. Thermal properties are indeed beneficial, but colloidal stability was a challenge, and this may be intrinsic to the PMMA. Follow-up experiments are required to test the PMMA stability with the tailored ratio between the reactant amounts. At the moment, PS is preferred as a template material, even though the thermal properties of PMMA are superior. PS has shown more promising results in the gold seeding step.

In the second step, gold seeding on the template particles showed, using the original method, in the first instance, adequate results. Gold nanoparticles were inhomogeneously distributed, but seeding on the surface was successful, and colloidal stability seemed unaffected. Scaling up the synthesis appeared to disrupt the colloidal stability of the system, due to the mismatch between the amount of template material and $SnCl_2$. By adapting the method and recalculating the ratios of reactants, colloidal stability no longer posed a problem, and again, seeding was successful.

The amount of reducing agent, the amount of gold precursor, and the ratio between the reactants have been shown to affect the outcome of the synthesis. When the amount of reducing agent is decreased, the gold NPs increase in size, lowering the surface coverage of the template particle. When no reducing agent is added, the gold NPs become very small and evenly distributed over the template surface, which is a result of the reduction by the Sn^{2+} nucleation islands. Decreasing the amount of gold precursor leads to a decrease in the average gold NP size. Working with an amount of template material and $SnCl_2$ close to the desired ratio (42 mg $SnCl_2$ to $4 \cdot 10^{16}$ nm² of template surface) is expected to deliver more desired results, such as a

homogeneous distribution of gold NPs over the surface. A ratio close to zero leads to very few and very small gold NPs on the surface. A ratio around 1 mg $SnCl_2/10^{16}$ nm² template material seems to deliver small gold NPs, evenly distributed over the template surface and almost fully covering it. Ratios > 1 mg $SnCl_2/10^{16}$ nm² lead to the growth of particles and a decrease in surface coverage. This confirms our hypothesis that control over Au particle size, loading, and homogeneous (random) distribution is obtainable via the ratio of Sn^{2+} and the amount of template material.

UV-Vis spectra showed the plasmon resonance of the gold nanoparticles, around 530-550 nm. A red shift of all samples was noted, which is annotated with the higher refractive index of PS. Shifts in the localized surface plasmon resonance are observed, but no consistency between the particle size and the wavelength of peak absorption could be found, because of intrinsic size effects that occur at such sizes. The bandwidth did show a correlation with the average particle size; a larger particle size is correlated with smaller bandwidths. The visually observed size variation is also assumed to be playing a role here.

An attempt was made to synthesize a nanoshell; the TEM result showed that the synthesis was unsuccessful in the formation of a full nanoshell. Already existing gold NPs did not seem to have grown; rather, new gold NPs were formed, leading to a decrease in average particle size.

Seeding on PMMA template particles proved difficult due to colloidal instability. The imbalance between reactant amounts is assumed to be the main reason for this instability.

The method used here, using Sn^{2+} nucleation islands for gold decoration, also shows promise because several reaction parameters allow for the tailoring of the outcome of the synthesis. This makes the method flexible for the desired properties like control over gold NP size and loading, and a homogeneous (random) distribution over the template surface.

A follow-up study could be done to gain a better insight into this system's synthesis process and optical properties. For the first two steps, it is proposed that:

(1) A more in-depth study of the size variation in the template synthesis could be done to achieve precise control of particle diameter, which affects the surface charge density and thus the colloidal stability and Sn^{2+} nucleation for gold seeding. Zetapotential measurements could be done here to correlate surface charge to particle diameter.

(2) Zetapotential measurements can be coupled to a systematic study of the ratio between the amount of template material and $SnCl_2$. This is lacking in this study.

(3) A systematic study to optimize the gold seeding. Variation of the different reaction parameters, with relevant characterization, to study the effect of these parameters on the outcome of the synthesis. Homogeneous sizes and distribution over the surface of the gold nanoparticles should be the aim. Parameters that could be adjusted are the amount and type of reducing agent, the amount of gold precursor, and the ratio between added $SnCl_2$ and template surface area. And most importantly is to find a balance between these ratios, rather than optimizing them each independently.

Also, the envisioned synthesis pathways could be completed, obtaining gold-decorated titania nanoshells. A study of this material’s optical properties and photocatalytic performance towards the reverse water-gas shift reaction could then be done.

4. Experimental procedures and methods

4.1. General workflow

A hard templating method was used to realize these hollow nanostructures.[41, 50] Hard templates, here polymer particles, were first synthesized. An emulsion polymerization process in water was carried out to synthesize PS and PMMA particles. The polymerization was performed under an inert atmosphere (Ar) to prevent unwanted initiation or termination by oxygen radicals. After the synthesis of the templated, gold NPs were grown on the polymer particles in a gold seeding step, where Sn^{2+} ions were used as nucleation sites for gold seeding and tetrachloroauric acid ($HAuCl_4$) as a source of gold. Seeding was done using formaldehyde as a reducing agent. These steps were also carried out in water. An additional gold plating step was performed to obtain gold nanoshells. The PS synthesis, gold seeding, and gold plating procedures were based on developed methods by Mann D. et al.[22, 46]

4.2. Emulsion polymerization of styrene and methyl methacrylate

The method for both monomers was the same, except for the surfactants used, and based on developed methods applied by Mann D., et al., and a practical course in polymer chemistry from RWTH Aachen.[22, 46, 68]

Degassed water (90 ml) was placed in a Schlenk flask and evacuated using a Schlenk line setup (Figure S1). To remove the stabilizer, styrene/methyl methacrylate (Merck, stabilized/Aldrich Chemistry, stabilized) was slowly added over a fritted glass funnel (Figure S1), acting as a column, using Al_2O_3 (thermo scientific, 99%, micron APS powder, 200 m^2/g) as a stationary phase and filter paper to protect the fritted glass. Destabilized styrene/methyl methacrylate (25 ml) was then added to the evacuated Schlenk flask, further evacuating the resulting emulsion for 10 minutes. The surfactant (2.3 g) (sodium dodecyl sulfate (Merck) for PS[22, 46]; Disponil FES 32 for PMMA[69]) was added to the emulsion under Ar counterflow. The stable emulsion was then added to a 250 ml three-neck flask, flushed with Ar, and sealed with rubber septa (Figure S1). The emulsion was heated to 72°C. After a temperature control of 5 to 10 minutes, the initiator solution (380 mg potassium peroxodisulfate (Merck) in 10 ml deionized water) was added through the septum using a syringe. The reaction mixture was stirred (1100 rounds per minute (rpm)) at 72°C for 3 hours, after which the mixture was left to cool down and stored in sealed glass jars. DLS (Malvern Zetasizer Nano series, Nano-ZS90) was performed using disposable cuvettes to obtain particle sizes. Sample preparation involved diluting the obtained dispersions with deionized water. Solid weight content was determined with a moisture analyzer (Halogen Moisture Analyzer HE53), with a temperature setting of 120°C. TEM analysis was measured with a FEI Tecnai G2 Spirit Twin with a 120 kV accelerating voltage.

The sample consisted of an aqueous dispersion of PS or PMMA, diluted in ethanol (Fischer, ≥99.8%) and deposited on a carbon-coated copper grid with a Formvar film. Particle size distributions (lognormal) were obtained using TEM Imaging & Analysis (TIA) software for size measurements, calculations were done using Excel, and plots were made with Origin 2019b 64-bit. TGA was performed using a Discovery TGA (TA Instruments). Samples were loaded in platinum pans and ramped at 10°C/min to 600°C under N_2 with a 20 mL/min flow rate.

4.3. Gold NP seeding on polymer template particles

Here, the original and final adapted experimental methods will be considered in detail. We refer to section 2.2 for a detailed discussion of the gold seeding synthesis method and its adaptation. PS1 is used here; for the other polymer templates, the added amounts were recalculated based on molar ratios (Table S4). TEM analysis was measured with a FEI Tecnai G2 Spirit Twin with a 120 kV accelerating voltage. The sample consisted of an aqueous dispersion of gold-functionalized PS or PMMA, diluted in ethanol (Fischer, ≥99.8%), and deposited on a carbon-coated copper grid with a Formvar film. Particle size distributions (lognormal) were obtained using TEM Imaging & Analysis (TIA) software for size measurements, calculations were done using Excel, and plots were made with Origin 2019b 64-bit. UV-Vis spectra were collected using a Cary 5000 UV-Vis-NIR Spectrophotometer (Agilent Technologies). Absorption measurements of the obtained dispersions were done using disposable cuvettes. A wavelength range of 350-800 nm was chosen. Wavelength of peak absorption was calculated using the derivative in Origin 2019b 64-bit.

4.3.1. Original method

PS1 (20.36%, 2.725 mg, 13.18 µl) was added to a solution of $SnCl_2$ (Sigma-Aldrich, 98%) (42 mg) and HCl (VWR Chemicals) (100 µl, 37%) in deionized water (20 ml). The mixture was stirred for 1h. After 1h, it was centrifuged three times at room temperature, at 6000 rpm, for 30 minutes, and redispersed in deionized water (20 ml). The resulting dispersion was added to a freshly made solution of $HAuCl_4$ (Sigma-Aldrich, 99.995%, trihydrate) (5 mg) and K_2CO_3 (Merck, ≥99.0%) (5 mg) in deionized water (20 ml). After this, an aqueous formaldehyde solution (100 ml) (Merck, 37%, stabilized with 10% methanol) (diluted to 2%) was added. The final mixture was stirred for 1h at 80°C. After 1h, it was cooled down, centrifuged for 30 minutes at room temperature and 6000 rpm, and redispersed in deionized water (20 ml).

4.3.2. Calculation for the adaptation of the method

The adaptation of the method is based on the surface area per mass unit (A/m) of template material and concentration of the template material. Here, the case of PS1 is discussed, but the method is completely analogous for the other PS and PMMA samples. The surface area per mass unit is obtained by calculating the surface area of one particle (Equation 1), the volume of one particle (Equation 2), and using the density of PS ($\rho = 1.05\ g \cdot ml^{-1}$). Using Equation 3, the surface area per mass unit can be calculated. For PS1, a value of $1.05 \cdot 10^{17}$ nm^2/mg is obtained.

$$A = 4 \cdot \pi \cdot r^2 \quad (1)$$

$$V = (4/3) \cdot \pi \cdot r^3 \quad (2)$$

$$A/m = A/(V \cdot \rho) \quad (3)$$

In Reference 47, 42 mg of $SnCl_2$ was used for a total surface area of $4 \cdot 10^{16}$ nm^2; this is 11 mg $SnCl_2$ per 10^{16} nm^2 of template material. To obtain a similar ratio, 42 mg of $SnCl_2$ should be added to 0.378 mg of PS1, corresponding to 1.86 µl (20.36 wt%, 203.6 mg/ml, Table 2). For the final adapted method (see next section), 84 mg of $SnCl_2$ and 7.5 µl of PS1 were used.

4.3.3. Final adapted method

$Sn(II)Cl_2$ (84 mg) (Sigma-Aldrich, 98%) was dissolved in deionized water (40 ml). After this, HCl (200 µl) (VWR Chemicals) (37%) was added. PS1 (7.5 µl) (20.36%) was added to the solution. The mixture was stirred for 1h at room temperature. After 1h, it was centrifuged 2 times for 30 minutes at 10000 rpm, and redispersed in deionized water (40 ml). $HAuCl_4$ (10 mg) (Sigma-Aldrich, 99.995%, trihydrate) and K_2CO_3 (10 mg) (Merck, ≥99.0%) were dissolved in deionized water (40 ml). The dispersion of Sn-functionalized PS1 particles was added to the $HAuCl_4$-K_2CO_3 solution, and heated to 80°C. At 80°C, a 2% formaldehyde solution (200 µl) (Merck, 37%, stabilized with 10% methanol) was added. The resulting reaction mixture was stirred for 1h at 80°C. After this, it was cooled down, centrifuged for 30 minutes at room temperature and 2000 rpm, and redispersed in deionized water (20 ml).

4.4. Gold plating on seeded polymer template particles

$HAuCl_4$ (15 mg) (Sigma-Aldrich, 99.995%, trihydrate) and K_2CO_3 (60 mg) (Merck, ≥99.0%) were dissolved in deionized water (100 ml) and aged overnight to obtain a gold hydroxide solution. The gold-seeded polymer dispersion (10 ml) was mixed with the gold hydroxide solution (75 ml). The mixture was stirred for 1h at room temperature, whilst adding a solution of sodium borohydride (Acros Organics, 99%, VenPure™ SF powder) (2 mg in 7.5 ml water) dropwise (a separatory funnel was used) to the mixture during 1h. MPEG Thiol 6000 (Sigma-Aldrich, average Mn 6000) (2 mg in 10 ml water) was added, and the resulting reaction mixture

was centrifuged at room temperature for 30 minutes at 2000 rpm. TEM analysis was measured with a FEI Tecnai G2 Spirit Twin with a 120 kV accelerating voltage. The sample consisted of an aqueous dispersion of PS-supported gold nanoshells, diluted in ethanol (Fischer, ≥99.8%) and deposited on a carbon-coated copper grid with a Formvar film. UV-Vis spectra were collected using a Cary 5000 UV-Vis-NIR Spectrophotometer (Agilent Technologies). Absorption measurements of the obtained dispersions were done using disposable cuvettes. A wavelength range of 350-950 nm was chosen. Wavelength of peak absorption was calculated using the derivative in Origin 2019b 64-bit.

Acknowledgements

The work presented here was not accomplished alone; in this way, I would like to thank some people for their contributions, guidance, advice, and support.

Above all, I would like to thank Dr. Daniel Mann for his guidance, support, scientific insights, and expertise on the topic of this study. And especially to help adapt the gold seeding method. This endeavour would not have been possible without him. Special thanks to Prof. Dr. Pascal Buskens for his advice, scientific contributions, and feedback during the project. I am also thankful to Prof. Dr. Marlies K. Van Bael for her personal guidance and support, advice, and feedback on the project. Also, I'd like to thank Prof. Dr. Marlies K. Van Bael and Prof. Dr. Pascal Buskens for giving me the opportunity to work on this project.

I would like to recognize Esmee Roman for her aid in the lab and advice. Prof. Dr. Jan D'Haen, and Sander Stulens are also to be thanked, along with Esmee Roman, for the TEM measurements at imo-imomec.

Lastly, I would like to acknowledge my fellow students who accompanied me on this journey, especially Romy van Geijn. She offered valuable tips and shared her practical experiences, and our discussions often led to fruitful outcomes for which I am very grateful.

References

1. Richardson, K., et al., *Earth beyond six of nine planetary boundaries.* Science Advances, 2023. **9**(37): p. eadh2458.
2. IPCC, 2023: Climate Change 2023: Synthesis Report. Contribution of Working Groups I, II and III to the Sixth Assessment Report of the Intergovernmental Panel on Climate Change [Core Writing Team, H. Lee and J. Romero (eds.)]. IPCC, Geneva, Switzerland, 184 pp., doi: 10.59327/IPCC/AR6-9789291691647.
3. Aziz, M.A.A., et al., *A review of heterogeneous catalysts for syngas production via dry reforming.* Journal of the Taiwan Institute of Chemical Engineers, 2019. **101**: p. 139-158.
4. Detz, R., et al., *Towards the Use of Renewable Syngas for the Decarbonization of Industry.* ChemSusChem, 2024. **17**(15): p. e202400059.
5. Schuurmans, J.H.A., et al., *Solar-Driven Continuous CO2 Reduction to CO and CH4 using Heterogeneous Photothermal Catalysts: Recent Progress and Remaining Challenges.* ChemSusChem, 2024. **17**(4): p. e202301405.
6. Vu, N.-N., S. Kaliaguine, and T.-O. Do, *Plasmonic Photocatalysts for Sunlight-Driven Reduction of CO2: Details, Developments, and Perspectives.* ChemSusChem, 2020. **13**(16): p. 3967-3991.
7. Volders, J., et al., *Sunlight-Powered Reverse Water Gas Shift Reaction Catalysed by Plasmonic Au/TiO2 Nanocatalysts: Effects of Au Particle Size on the Activity and Selectivity.* Nanomaterials, 2022. **12**(23): p. 4153.
8. González-Castaño, M., B. Dorneanu, and H. Arellano-García, *The reverse water gas shift reaction: a process systems engineering perspective.* Reaction Chemistry & Engineering, 2021. **6**(6): p. 954-976.
9. Yu, S., et al., *Opportunities and Challenges of Solar-Energy-Driven Carbon Dioxide to Fuel Conversion with Plasmonic Catalysts.* ACS Energy Letters, 2017. **2**(9): p. 2058-2070.
10. Zhang, Y., et al., *Surface-Plasmon-Driven Hot Electron Photochemistry.* Chemical Reviews, 2018. **118**(6): p. 2927-2954.
11. Martínez Molina, P., et al., *Low Temperature Sunlight-Powered Reduction of CO2 to CO Using a Plasmonic Au/TiO2 Nanocatalyst.* ChemCatChem, 2021. **13**(21): p. 4507-4513.
12. Zhang, F., et al., *Recent Advances and Applications of Semiconductor Photocatalytic Technology.* Applied Sciences, 2019. **9**(12): p. 2489.

13. Wang, H., et al., *Semiconductor heterojunction photocatalysts: design, construction, and photocatalytic performances.* Chemical Society Reviews, 2014. **43**(15): p. 5234-5244.
14. Yang, X. and D. Wang, *Photocatalysis: From Fundamental Principles to Materials and Applications.* ACS Applied Energy Materials, 2018. **1**(12): p. 6657-6693.
15. Zhang, X., et al., *Plasmonic photocatalysis.* Reports on Progress in Physics, 2013. **76**(4): p. 046401.
16. Valenti, M., et al., *Plasmonic nanoparticle-semiconductor composites for efficient solar water splitting.* Journal of Materials Chemistry A, 2016. **4**(46): p. 17891-17912.
17. Baffou, G. and R. Quidant, *Nanoplasmonics for chemistry*. Chemical Society Reviews, 2014. **43**(11): p. 3898-3907.
18. Zhang, Z., *Plasmonic Photocatalysis*, in *Principles and Applications*. 2022, Springer Singapore. p. VIII, 91.
19. Motl, N.E., et al., *Engineering plasmonic metal colloids through composition and structural design.* Chemical Society Reviews, 2014. **43**(11): p. 3823-3834.
20. Ahlawat, M., D. Mittal, and V. Govind Rao, *Plasmon-induced hot-hole generation and extraction at nano-heterointerfaces for photocatalysis.* Communications Materials, 2021. **2**(1): p. 114.
21. Zhang, Z., et al., *Plasmon-Driven Catalysis on Molecules and Nanomaterials.* Accounts of Chemical Research, 2019. **52**(9): p. 2506-2515.
22. Mann, D., *Design, synthesis and characterization of Au and Ag nanoshells and Au semishells with tunable localized surface plasmon resonance*, in *Fakultät für Mathematik, Informatik und Naturwissenschaften der RWTH Aachen University*. 2018, Aachen University. p. 237.
23. Njoki, P.N., et al., *Size Correlation of Optical and Spectroscopic Properties for Gold Nanoparticles.* The Journal of Physical Chemistry C, 2007. **111**(40): p. 14664-14669.
24. Prodan, E., et al., *A Hybridization Model for the Plasmon Response of Complex Nanostructures.* Science, 2003. **302**(5644): p. 419-422.
25. Halas, N., *Playing with Plasmons: Tuning the Optical Resonant Properties of Metallic Nanoshells.* MRS Bulletin, 2005. **30**(5): p. 362-367.
26. Graf, C. and A. van Blaaderen, *Metallodielectric Colloidal Core−Shell Particles for Photonic Applications.* Langmuir, 2002. **18**(2): p. 524-534.
27. Yong, K.-T., et al., *Synthesis and plasmonic properties of silver and gold nanoshells on polystyrene cores of different size and of gold–silver core–shell nanostructures.*

Colloids and Surfaces A: Physicochemical and Engineering Aspects, 2006. **290**(1): p. 89-105.

28. Li, W., et al., *Platinum and Frustrated Lewis Pairs on Ceria as Dual-Active Sites for Efficient Reverse Water-Gas Shift Reaction at Low Temperatures.* Angewandte Chemie, 2023. **135**(37): p. e202305661.
29. Feng, L. and J.-X. Liu, *Identification of Active Sites for Reverse Water–Gas Shift Reactions on Pt/TiO2 Cluster Catalysts.* Precision Chemistry, 2025.
30. Liang, C., et al., *Size-Dependent Catalytic Behavior of Gold Nanoparticles.* Advanced Materials Interfaces, 2022. **9**(4): p. 2100867.
31. Sun, D., et al., *Hollow Gold Nanoshells for Sensitive 2D Plasmonic Sensors.* ACS Applied Nano Materials, 2024. **7**(5): p. 5093-5102.
32. Hong, Y.A. and J.W. Ha, *Enhanced refractive index sensitivity of localized surface plasmon resonance inflection points in single hollow gold nanospheres with inner cavity.* Scientific Reports, 2022. **12**(1): p. 6983.
33. Ghosh Chaudhuri, R. and S. Paria, *Core/Shell Nanoparticles: Classes, Properties, Synthesis Mechanisms, Characterization, and Applications.* Chemical Reviews, 2012. **112**(4): p. 2373-2433.
34. Awazu, K., et al., *A Plasmonic Photocatalyst Consisting of Silver Nanoparticles Embedded in Titanium Dioxide.* Journal of the American Chemical Society, 2008. **130**(5): p. 1676-1680.
35. Tahir, B., M. Tahir, and N.A.S. Amin, *Photocatalytic CO2 conversion over Au/TiO2 nanostructures for dynamic production of clean fuels in a monolith photoreactor.* Clean Technologies and Environmental Policy, 2016. **18**(7): p. 2147-2160.
36. Rahman, Z.U., et al., *Synthesis of Hollow Mesoporous TiO2 Microspheres with Single and Double Au Nanoparticle Layers for Enhanced Visible-Light Photocatalysis.* Chemistry – An Asian Journal, 2018. **13**(4): p. 432-439.
37. Wang, L., M.H. Kafshgari, and M. Meunier, *Optical Properties and Applications of Plasmonic-Metal Nanoparticles.* Advanced Functional Materials, 2020. **30**(51): p. 28.
38. Shehzad, N., et al., *A critical review on TiO2 based photocatalytic CO2 reduction system: Strategies to improve efficiency.* Journal of CO2 Utilization, 2018. **26**: p. 98-122.
39. Li, W., et al., *A Perspective on Mesoporous TiO2 Materials.* Chemistry of Materials, 2014. **26**(1): p. 287-298.

40. Joo, J.B., et al., *Mesoporous Anatase Titania Hollow Nanostructures though Silica-Protected Calcination.* Advanced Functional Materials, 2012. **22**(1): p. 166-174.
41. Wang, X., et al., *Synthesis, Properties, and Applications of Hollow Micro-/Nanostructures.* Chemical Reviews, 2016. **116**(18): p. 10983-11060.
42. Xu, M., et al., *Using Fiber Bragg Grating Sensors to Quantify Temperature Non-Uniformities in Plasmonic Catalyst Beds under Illumination.* ChemPhotoChem, 2022. **6**(4): p. e202100289.
43. Sivan, Y. and Y. Dubi, *Recent developments in plasmon-assisted photocatalysis—A personal Perspective.* Applied Physics Letters, 2020. **117**(13).
44. Lou, X.W., L.A. Archer, and Z. Yang, *Hollow Micro-/Nanostructures: Synthesis and Applications.* Advanced Materials, 2008. **20**(21): p. 3987-4019.
45. Sarfraz, N. and I. Khan, *Plasmonic Gold Nanoparticles (AuNPs): Properties, Synthesis and their Advanced Energy, Environmental and Biomedical Applications.* Chemistry – An Asian Journal, 2021. **16**(7): p. 720-742.
46. Mann, D., et al., *Glucose-functionalized polystyrene particles designed for selective deposition of silver on the surface.* RSC Advances, 2014. **4**(108): p. 62878-62881.
47. Mann, D., et al., *The Influence of Particle Size Distribution and Shell Imperfections on the Plasmon Resonance of Au and Ag Nanoshells.* Plasmonics, 2017. **12**(3): p. 929-945.
48. Timothy P. Lodge, P.C.H., *Polymer Chemistry*. 3 ed. 2020: CRC Press. 661.
49. Liu, X., et al., *Understanding ceiling temperature as a predictive design parameter for circular polymers.* Cell Reports Physical Science, 2024. **5**(4): p. 101910.
50. Yu, L., X.Y. Yu, and X.W. Lou, *The Design and Synthesis of Hollow Micro-/Nanostructures: Present and Future Trends.* Advanced Materials, 2018. **30**(38): p. 1800939.
51. Lomakin, S.M., et al., *An investigation of the thermal stability and char-forming tendency of cross-linked poly(methyl methacrylate).* Polymer Degradation and Stability, 1993. **41**(2): p. 229-243.
52. Ferriol, M., et al., *Thermal degradation of poly(methyl methacrylate) (PMMA): modelling of DTG and TG curves.* Polymer Degradation and Stability, 2003. **79**(2): p. 271-281.
53. Cheng, J., et al., *Mechanisms and kinetics studies on the thermal decomposition of micron Poly (methyl methacrylate) and polystyrene.* Journal of Loss Prevention in the Process Industries, 2016. **40**: p. 139-146.

54. Lovell, P.A. and F.J. Schork, *Fundamentals of Emulsion Polymerization.* Biomacromolecules, 2020. **21**(11): p. 4396-4441.
55. GmbH, N.T., *The biologics researcher's guido to DLS*. NanoTemper Technologies GmbH. p. 63.
56. BASF, *Disponil BES/FES alkyl ethersulfates*. 2013.
57. BASF, *BASF Industrial Formulators*. 2021.
58. Mukerjee, P. and K. Mysels, *Critical micelle concentrations of aqueous surfactant systems*. 1971, , National Institute of Standards and Technology, Gaithersburg, MD.
59. Asandulesa, M., et al., *Thermal and Dielectric Investigations of Polystyrene Nanoparticles as a Viable Platform—Toward the Next Generation of Fillers for Nanocomposites.* Polymers, 2023. **15**(13): p. 2899.
60. Prime, R.B., et al., *Thermogravimetric Analysis (TGA)*, in *Thermal Analysis of Polymers*. 2009. p. 241-317.
61. De Vries, K.J. and P.J. Gellings, *The thermal decomposition of potassium and sodium-pyrosulfate.* Journal of Inorganic and Nuclear Chemistry, 1969. **31**(5): p. 1307-1313.
62. Chang, C.-P., et al., *Growth mechanism of gold nanoparticles decorated on polystyrene spheres via self-regulated reduction.* Colloid and Polymer Science, 2010. **288**(4): p. 395-403.
63. van den Berg, R., et al., *Support Functionalization To Retard Ostwald Ripening in Copper Methanol Synthesis Catalysts.* ACS Catalysis, 2015. **5**(7): p. 4439-4448.
64. Yin, P., et al., *Quantification of critical particle distance for mitigating catalyst sintering.* Nature Communications, 2021. **12**(1): p. 4865.
65. Amendola, V., et al., *Surface plasmon resonance in gold nanoparticles: a review.* Journal of Physics: Condensed Matter, 2017. **29**(20): p. 203002.
66. Norman, T.J., et al., *Near Infrared Optical Absorption of Gold Nanoparticle Aggregates.* The Journal of Physical Chemistry B, 2002. **106**(28): p. 7005-7012.
67. Link, S. and M.A. El-Sayed, *Size and Temperature Dependence of the Plasmon Absorption of Colloidal Gold Nanoparticles.* The Journal of Physical Chemistry B, 1999. **103**(21): p. 4212-4217.
68. Möller, M., *Polymerchemisches Praktikum für Studierende des Maschinenbaus*. Institut für Technische Chemie und Makromolekulare Chemie: RWTH Aachen. p.26-29.
69. Guillemot, F., et al., *Latex-Templated Silica Films: Tailoring Porosity to Get a Stable Low-Refractive Index.* Chemistry of Materials, 2010. **22**(9): p. 2822-2828.

Supporting information

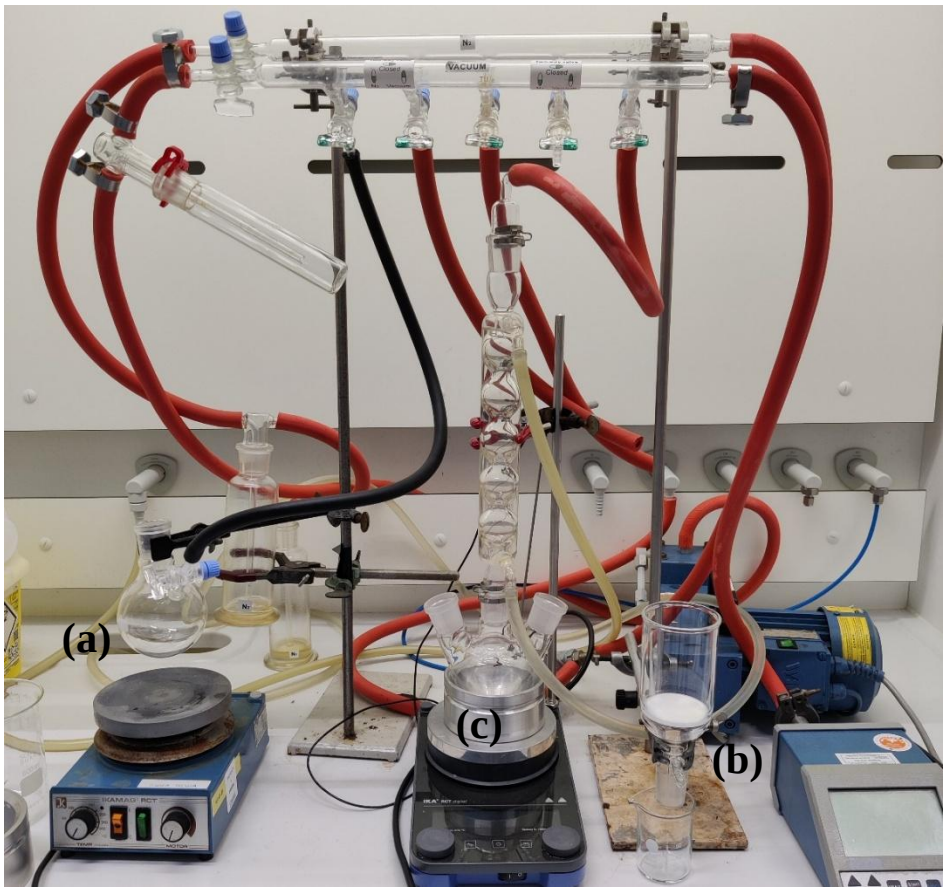

Figure S1. Picture of the Schlenk line setup for the emulsion polymerization of styrene and methyl methacrylate. Schlenk flask for degassing of water and monomer solution (a). Fritted glass funnel, for the destabilization of styrene and methyl methacrylate (b). Three-neck flask with cooler for the emulsion polymerization of destabilized styrene and methyl methacrylate (c).

Figure S2. Picture of the obtained samples from the emulsion polymerizations of destabilized styrene. From left to right: PS1-2-3-4-5.

Figure S3. Picture of the obtained samples from the emulsion polymerizations of destabilized methyl methacrylate. From left to right: PMMA1-2-3-4.

Table S1. Overview of the parameters in the synthesis of PS and PMMA.

Sample	Volume monomer [ml]	Volume degassed water [ml]	Mass surfactant [g]	Mass initiator [g]	Stirring rate [rpm]4[a]
PS1	25	90	2.3030	0.3830	1100
PS2	25	90	2.3022	0.3847	1100
PS3	25	90	2.3058	0.3846	1100
PS4	25	90	1.1521	0.3794	1100
PS5	50	180	2.3157	0.2310	800
PMMA1	25	90	2,3386	0.3862	1100
PMMA2	25	90	2,3350	0.3813	1100
PMMA3	50	180	2,3053	0.3807	1100
PMMA4	50	180	2,3155	0.3839	1100

a) For all syntheses, except PS5, the same magnetic stirring bar was used. For PS5, a larger stirring bar was used, so the rate was set lower.

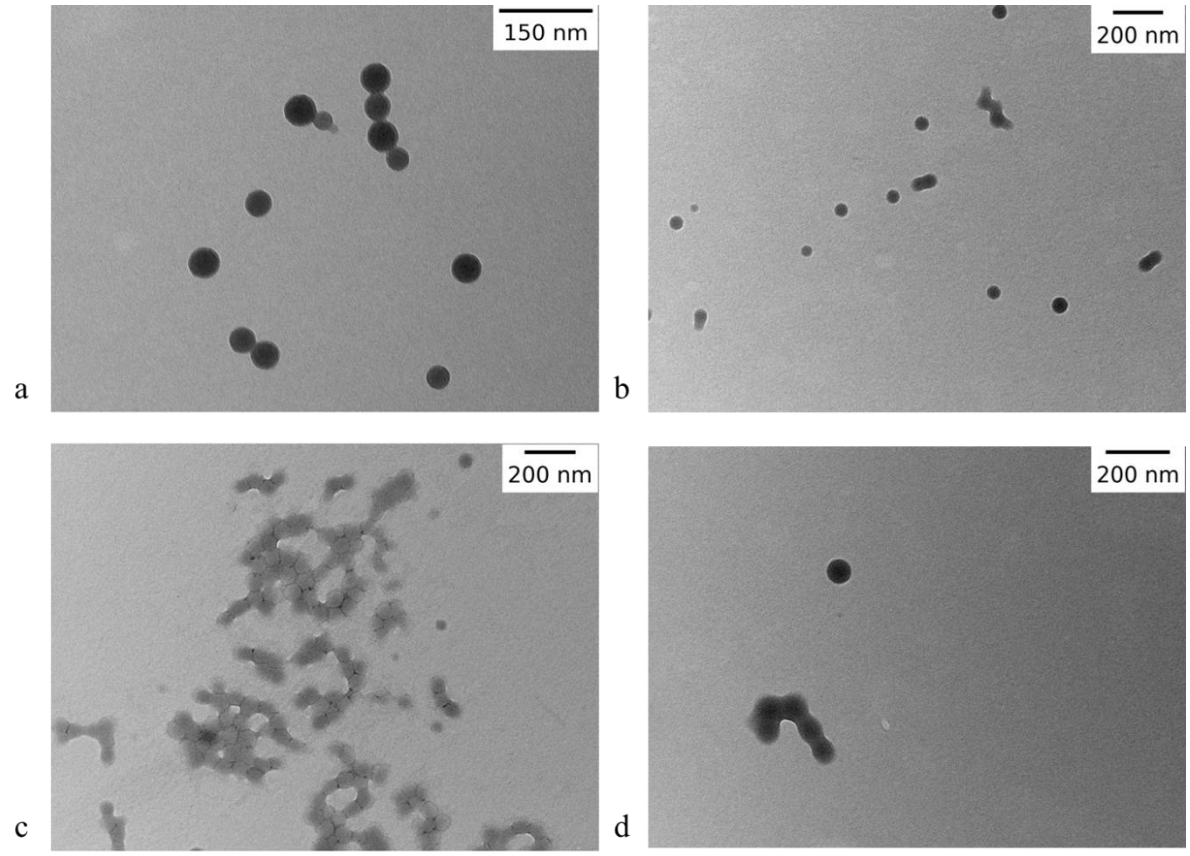

Figure S4. TEM images of samples PS4 (a), PMMA2 (b), PMMA1 (c), and PMMA4 (d).

Table S2. PS1 average particle size determined via TEM.

Number of particles measured	Average particle size [nm]	Standard deviation [nm]	90% confidence interval [nm]
132	48.7	5.4	0.8

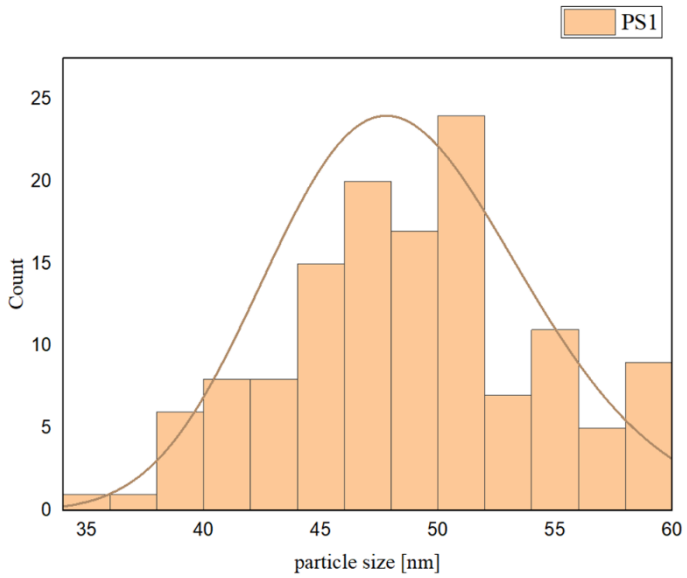

Figure S5. Particle size distribution of PS1.

Table S3. Initial weight, residual weight, and weight percentage of the TGA performed on PS and PMMA.

Sample	Initial weight [mg]	Residual weight [mg]	Weight % [%]
PS Nitrogen	19.585	0.504	2.575
PS Air	27.913	0.692	2.477
PMMA Nitrogen	18.307	0.383	2.092
PMMA Air	16.566	0.274	1.653

Table S4. Overview of the syntheses and parameters in the gold seeding.

Sample[d]	**Amount of template**	**m($SnCl_2$) [g]**	**V(HCl) [ml]**	**m($HAuCl_4$) [g]**	**m(K_2CO_3) [g]**	**V(HCOH) [ml] (x %)**
PS1-Au-1	10.46 µl	0.0434	0.1	0.0134	0.014	100.00 (2%)
PS1-Au-2[a]	4.3893 g	1.052	2.5			21.640 (37%)
PS1-Au-3[a]	4.3992 g	1.052	2.5			21.640 (37%)
PS1-Au-5[b]						
PS1-Au-6	7.5 µl	0.0881	0.2	0.0118	0.0101	0.000
PS1-Au-7	7.5 µl	0.0839	0.2	0.0162		0.100 (2%)
PS1-Au-8	15 µl	0.1702	0.4	0.0126	0.0152	0.200 (2%)
PS2-Au-1[a]	0.1416 g	0.5211	1.25	0.0683	0.0637	100.00 (2%)
PS3-Au-1[a,c]	4.3708 g	2.629	1.2			
PS3-Au-2[a,c]	4.3901 g	5.2684	2.35			
PS3-Au-3[a,c]	4.3699 g	26.5281	11.75			
PS5-Au-1[a]	4.3703 g	1.055	2.5	0.1292	0.126	21.64 (37%)
PS5-Au-2[a,c]	4.3920 g	1.0528	2.5			
PS5-Au-3[a,c]	4.4103 g	1.062	1.25			
PS5-Au-4[a,c]	4.3775 g	1.5784	1.25			
PS5-Au-5[a,c]	4.3743 g	2.1079	1.25			
PS5-Au-6[a,c]	4.3743 g	2.629	1.20			

a) Use of $SnCl_2$-HCl and $HAuCl_4$-K_2CO_3 stock solutions (table S3).
b) First synthesis with adapted method (see section 4.3.3). Specific parameters were not noted.
c) Only the Sn deposition step was done.
d) Incompleteness of the table is due to a lack of consistently noting the method for the preparation of stock solutions.

Table S4. Continued.

Sample[d]	Amount of template	m($SnCl_2$) [g]	V(HCl) [ml]	m($HAuCl_4$) [g]	m(K_2CO_3) [g]	V(HCOH) [ml] (x %)
PS5-Au-7[a,c]	4.3743 g	5.2684	2.35			
PS5-Au-8[a]	1.8640 g	10.5481	4.7			
PS5-Au-9[a,c]	4.3861 g	26.5281	11.75			
PMMA1-Au-1[a]	0.0363 g	0.5211	1.25	0.0683	0.0637	21.64 (37%)
PMMA1-Au-2[a]	0.1063 g			0.0597	0.0628	21.64 (37%)
PMMA1-Au-3[a]	0.1081 g			0.0597	0.0649	21.64 (37%)
PMMA2-Au-1[a]	1.0950 g	0.5242	1.25			100 (2%)
PMMA3-Au-1[a]	4.3891 g	0.5188	1.25			21.64 (37%)
PMMA4-Au-1[a]	4.6038 g					21.64 (37%)
PMMA4-Au-2[a]	4.3623 g	1.0662	2.5			21.64 (37%)
PMMA4-Au-3[a]	4.3705	1.0662	2.5			21.64 (37%)
PMMA4-Au-4[a]	4.3858 g	1.0622	2.5			21.64 (37%)
PMMA4-Au-5[a]	4.3574 g	1.0662	2.5			21.64 (37%)

a) use of $SnCl_2$-HCl and $HAuCl_4$-K_2CO_3 stock solutions (table S3).
c) only Sn deposition step was done.
d) Incompleteness of the table is due to a lack of consistently noting the method for the preparation of stock solutions.

Table S5. Preparation of the stock solutions.

Stock solution	**Total volume [ml]**	**Solute 1 and amount**	**Solute 2 and amount**
$SnCl_2$ – HCl	250	$SnCl_2$ 525 mg	HCl (37%) 1.25 ml
$HAuCl_4$ – K_2CO_3	250	$HAuCl_4$ 62.5 mg	K_2CO_3 62.5 mg
HCOH	1000	HCOH (37%) 54.05 ml	N/A
Template dispersion stock[a]	500	PS2 50 ml	N/A

a) Only used for the synthesis of PS2-Au-1.

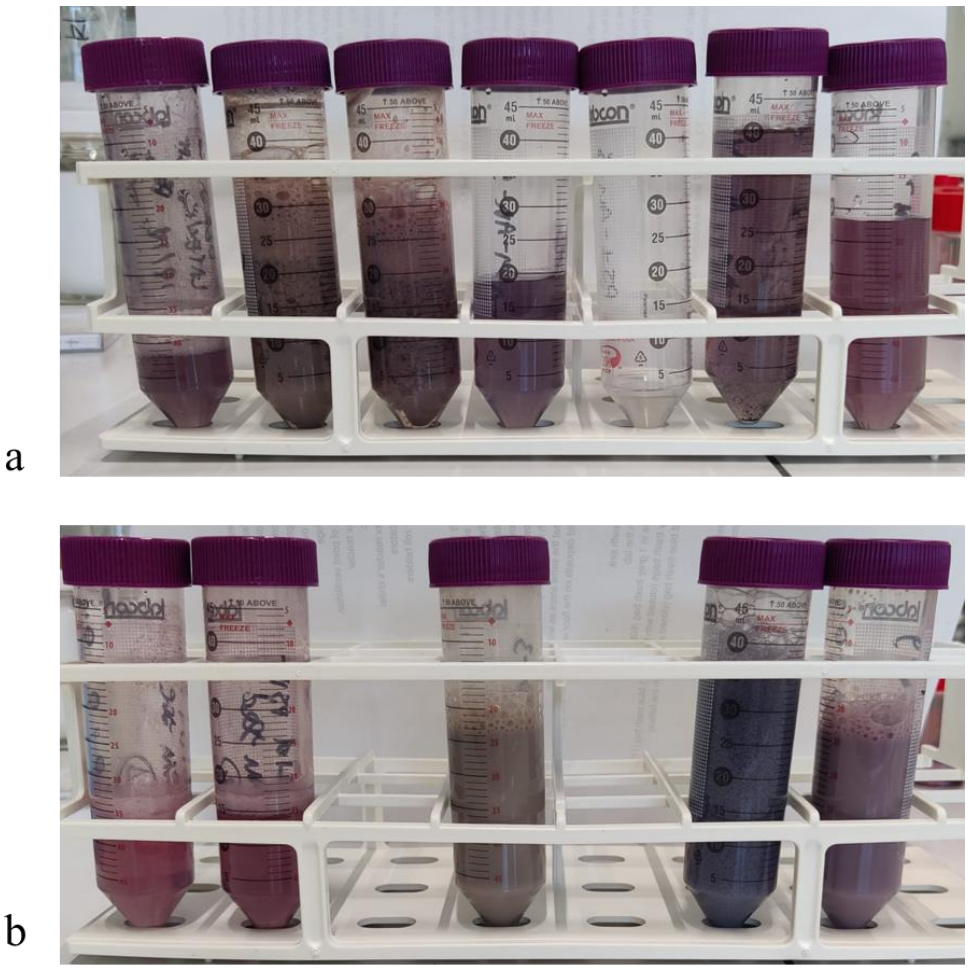

Figure S6. Pictures of the gold-seeded PS samples. From left to right: PS1-Au-1,2,3,5,6,7,8 (a), and PS2-Au-1,2; PS3-Au-3; PS5-Au-1,9 (b).

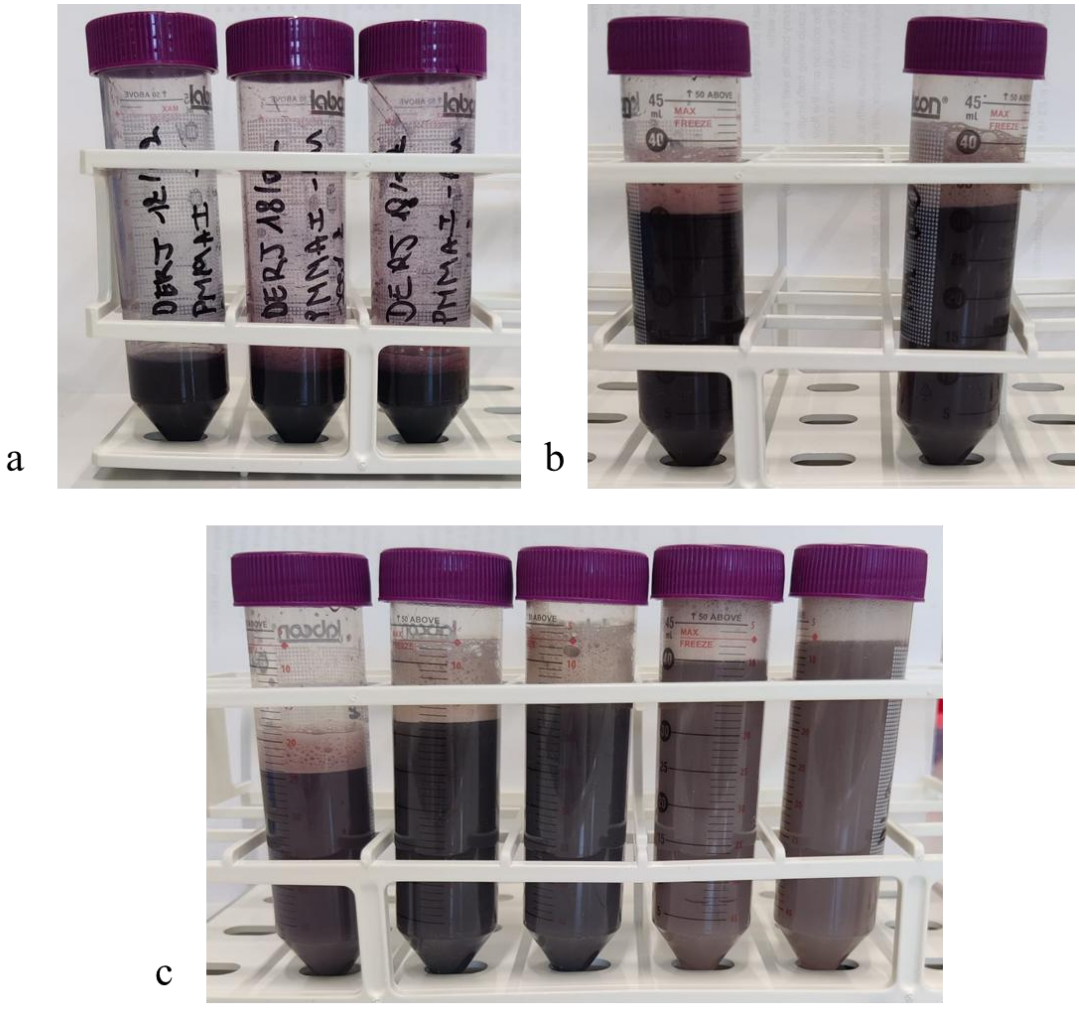

Figure S7. Pictures of the gold-seeded PMMA samples. From left to right: PMMA1-Au-1,2,3 (a), PMMA2-Au-1; PMMA3-Au-1 (b), and PMMA4-Au-1,2,3,4,5 (c).

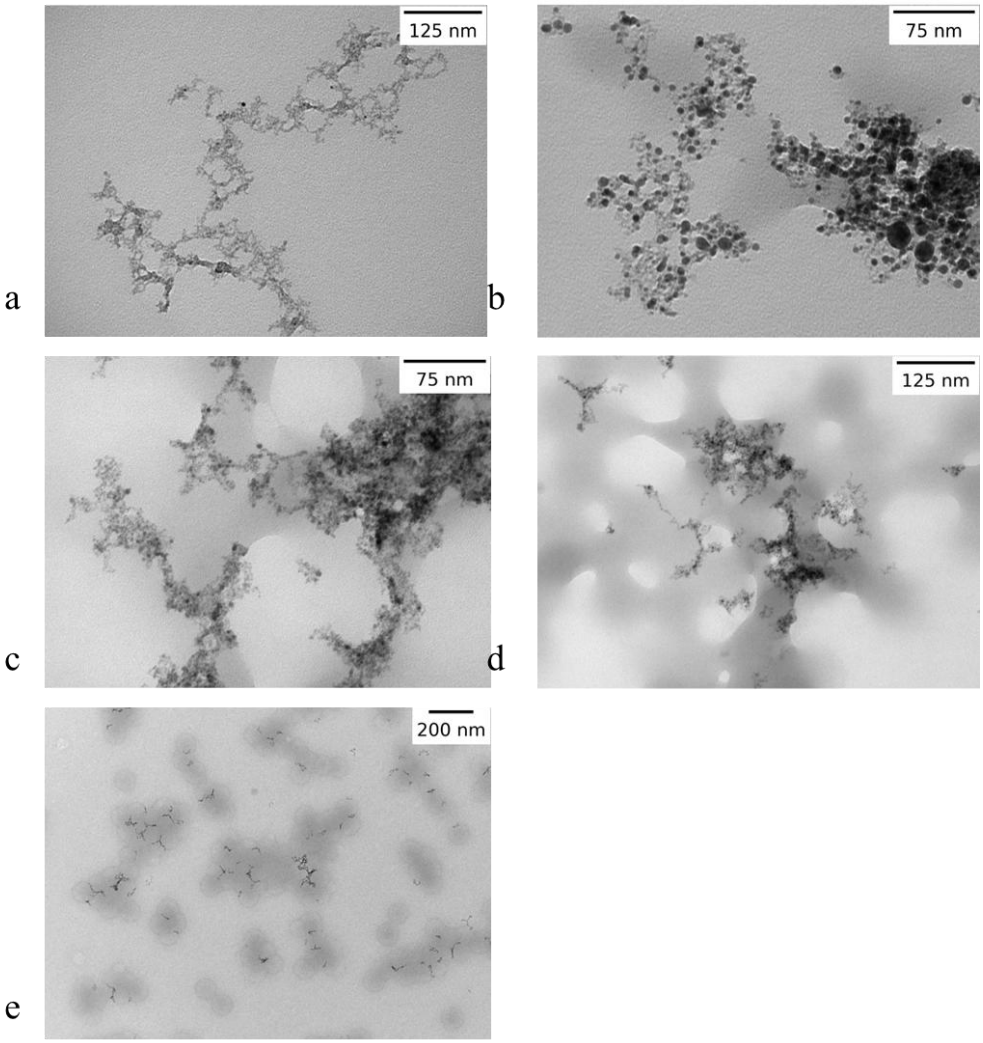

Figure S8. TEM images of samples PMMA1-Au-1 (a), PMMA1-Au-2 (b), PMMA2-Au-1 (c), PMMA3-Au-1 (d), and PMMA4-Au-1 (e).

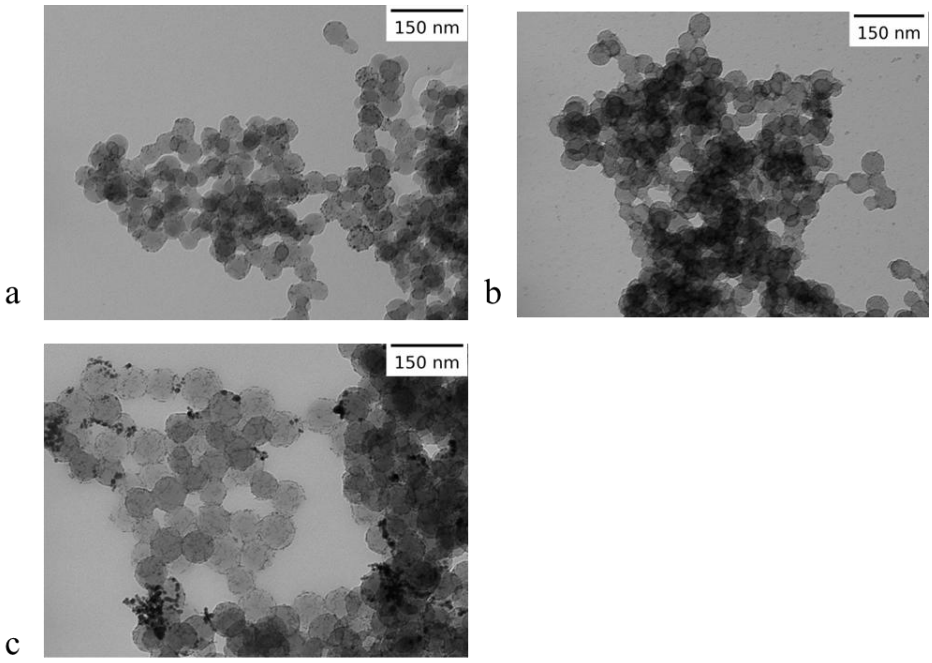

Figure S9. TEM images of samples PS1-Au-2 (a), PS3-Au-3 (b), and PS5-Au-1 (c).

Table S6. Overview of the parameters in the gold plating.

Sample	**m($HAuCl_4$) [mg][a]**	**m(K_2CO_3) [mg][a]**	**m($NaBH_4$) [mg]**
PS1-Au-5-NS1	14.8	59.1	2.4

a) Amounts for $HAuCl_4$-K_2CO_3 solution made beforehand, to obtain gold hydroxide solution.

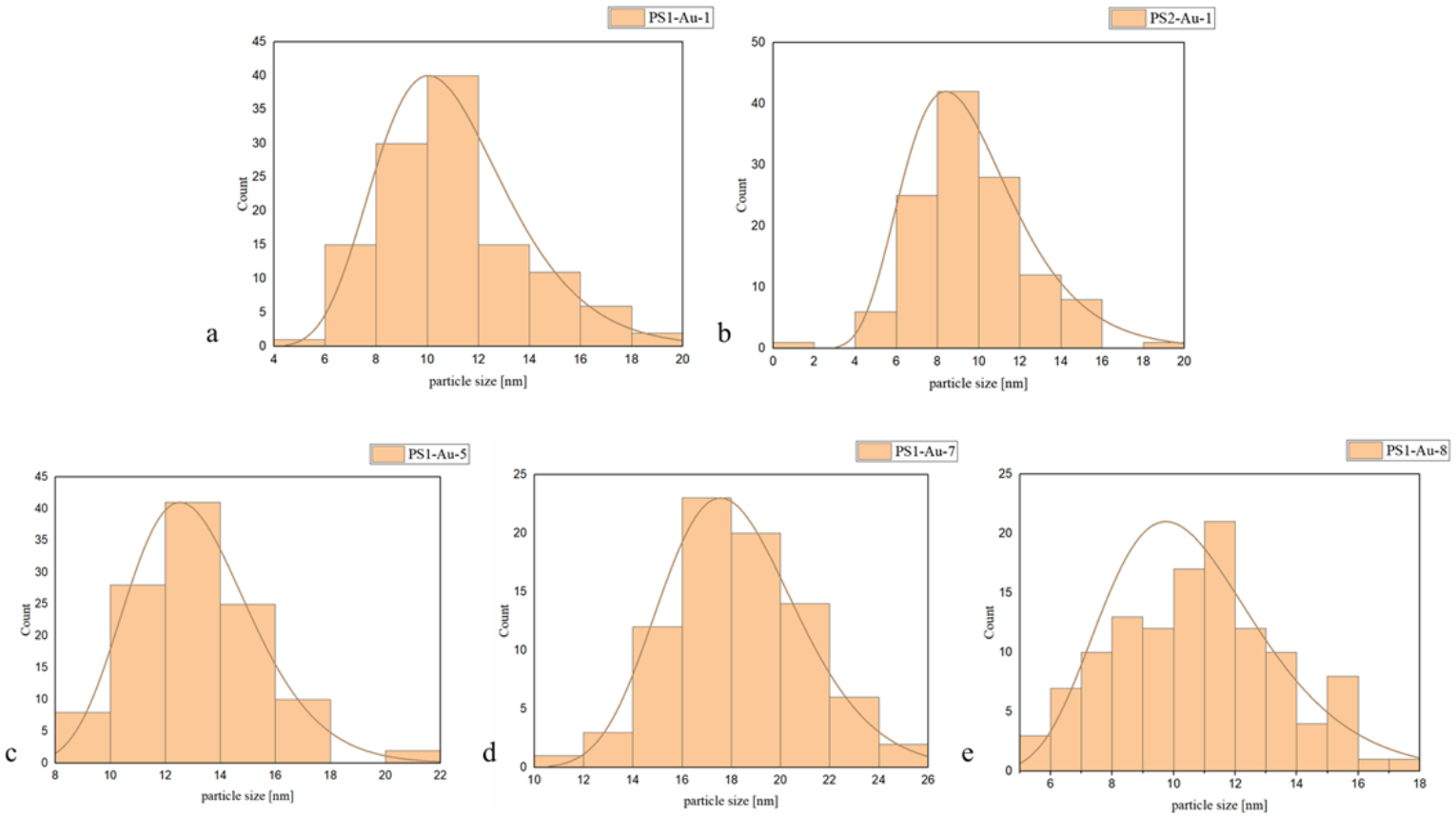

Figure S10. Particle size distributions for PS1-Au-1 (a), PS2-Au-1 (b), PS1-Au-5 (c), PS1-Au-7 (d), and PS1-Au-8 (e).

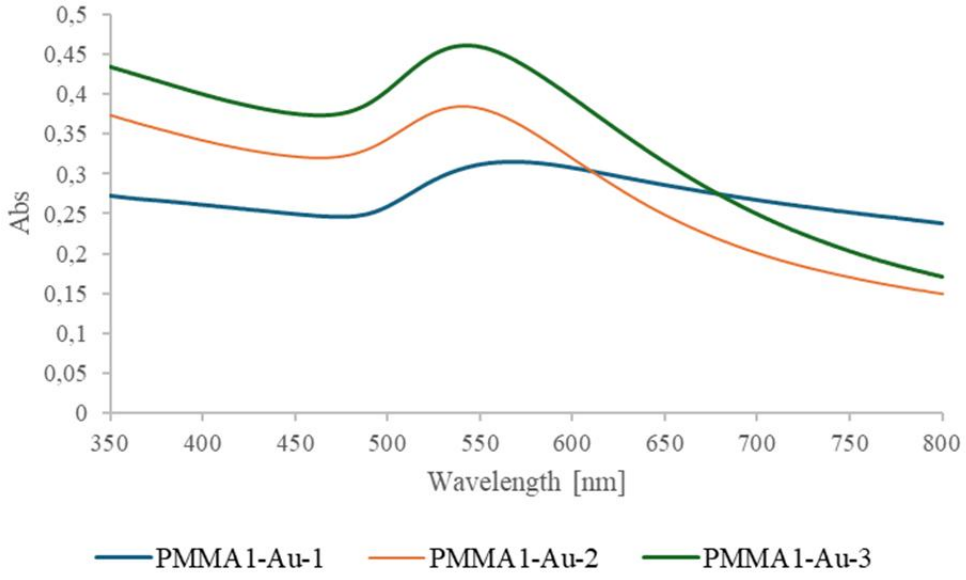

Figure S11. UV-Vis absorption spectra of samples PMMA1-Au-1,2,3.

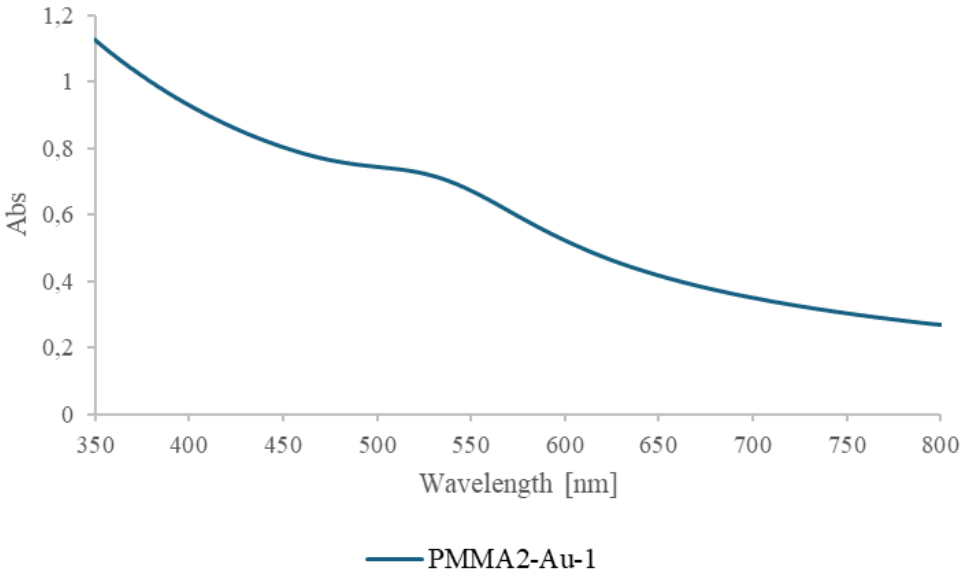

Figure S12. UV-Vis absorption spectrum of sample PMMA2-Au-1.

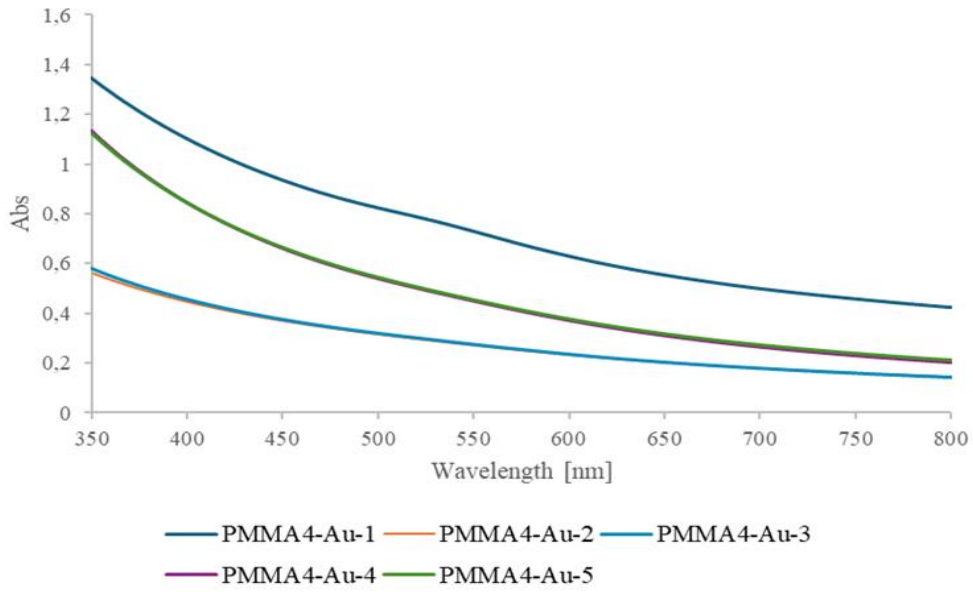

Figure S13. UV-Vis absorption spectra of samples PMMA4-Au-1,2,3,4,5.

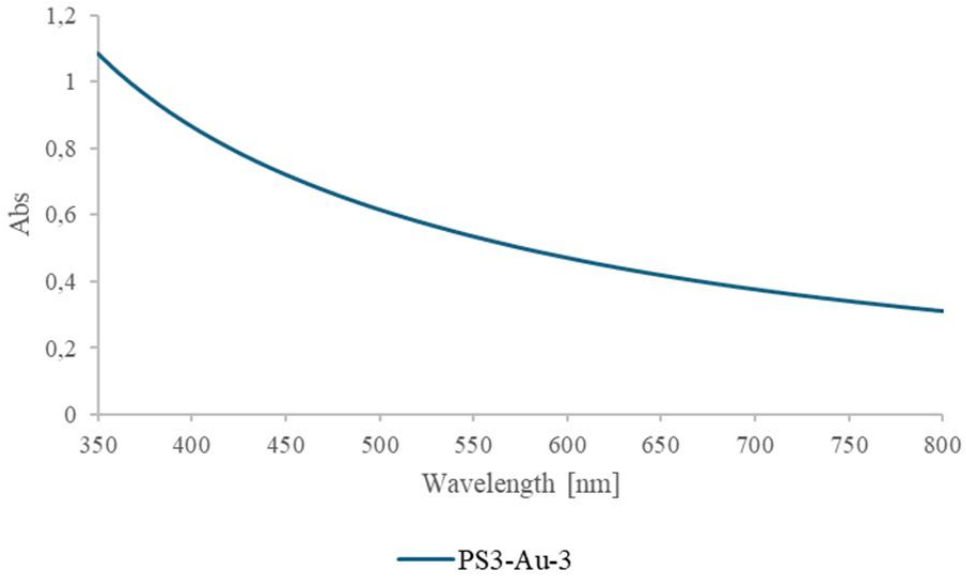

Figure S14. UV-Vis absorption spectrum of sample PS3-Au-3.

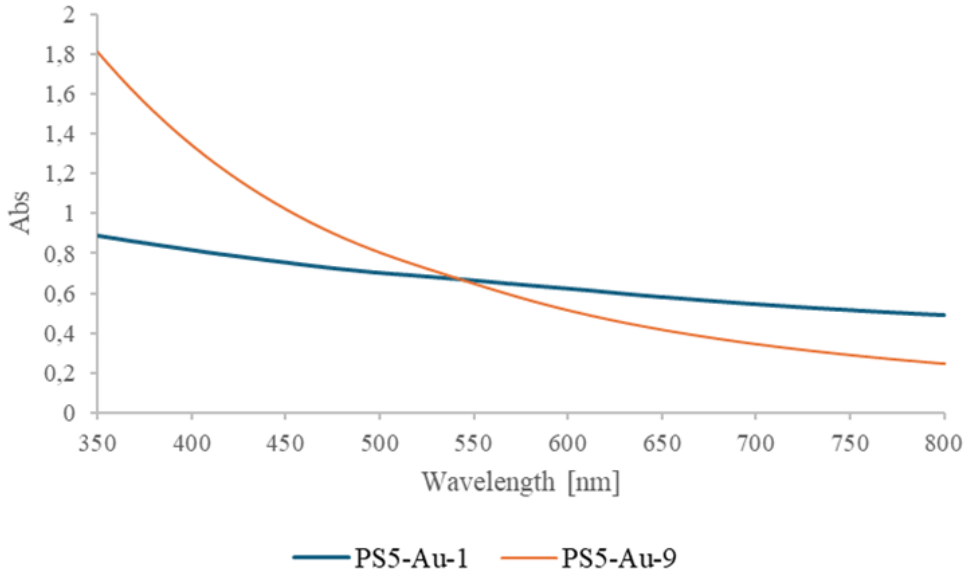

Figure S15. UV-Vis absorption spectrum of samples PS5-Au-1 and PS5-Au-9.

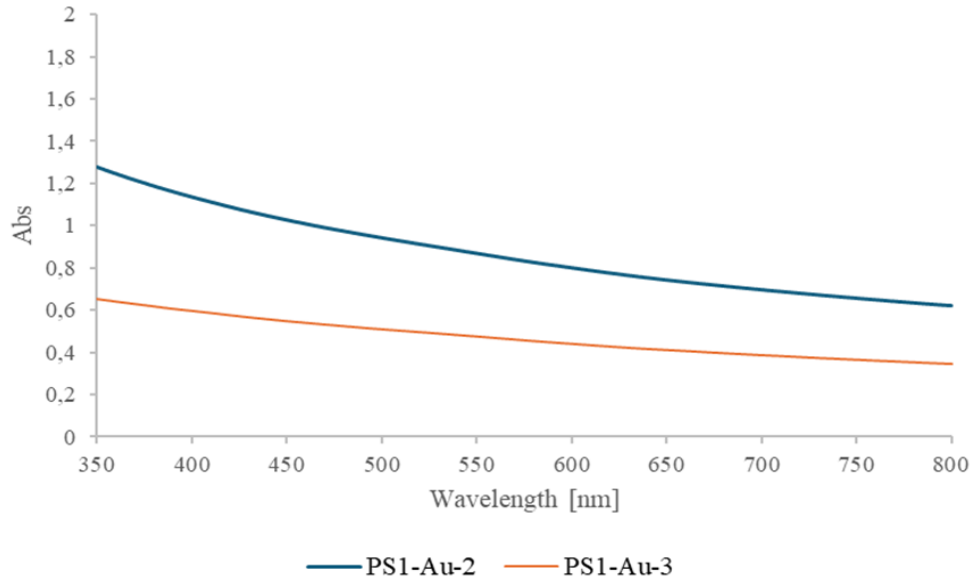

Figure S16. UV-Vis absorption spectra of samples PS1-Au-2 and PS1-Au-3.

Table S7. PS1-Au-5-NS average particle size determined via TEM.

Number of particles measured	Average particle size [nm]	Standard deviation [nm]	90% confidence interval [nm]
168	11.6	2.5	0.3

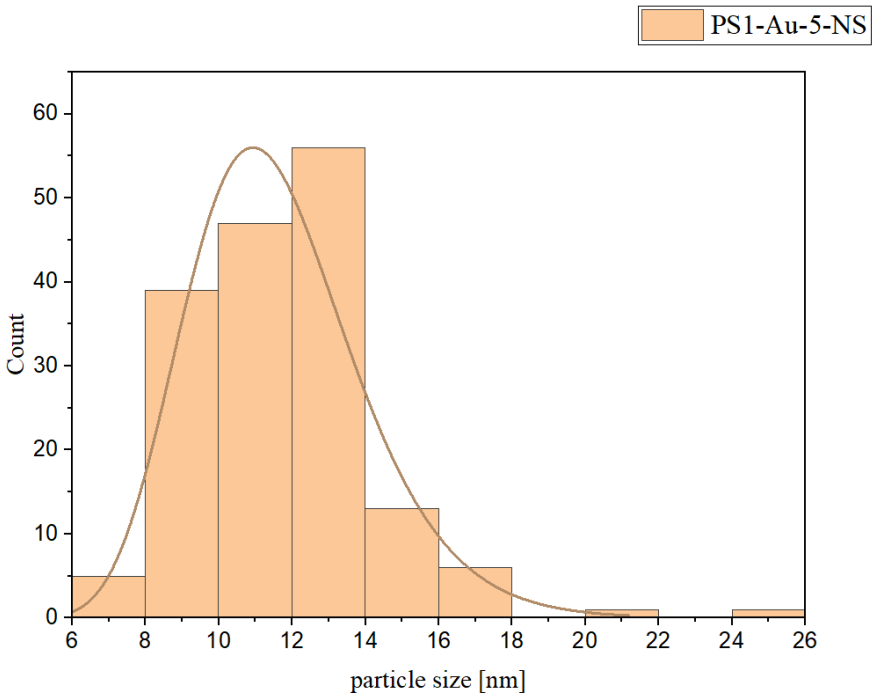

Figure S17. Particle size distribution of PS1-Au-5-NS.

Table S8. Calculated ratios of Sn per surface area of template material.

Sample	Ratio [mg $SnCl_2/10^{16}$ nm^2 template]
Aimed ratio	10.5
PS1-Au-1	1.93
PS1-Au-2	0.00893
PS1-Au-3	0.00891
PS2-Au-1	1.49
PS5-Au-1	0.0000149
PS5-Au-2	0.0148
PS5-Au-3	0.0149
PS5-Au-4	0.0223
PS5-Au-5	0.0297
PS5-Au-6	0.0371
PS5-Au-7	0.0744
PS5-Au-8	0.873
PS5-Au-9	1.02
PS1-Au-6	5.47
PS1-Au-7	5.21
PS1-Au-8	5.28
PMMA1-Au-1	0.760
PMMA1-Au-2	0.760
PMMA1-Au-3	0.760
PMMA2-Au-1	0.121
PMMA3-Au-1	0.0413
PMMA4-Au-1	0.0374
PMMA4-Au-2	0.0811
PMMA4-Au-3	0.0809
PMMA4-Au-4	0.0807
PMMA4-Au-5	0.0812